**Atmospheric
Measurement
Techniques**

Effects of ice particles shattering on the 2D-S probe

R. P. Lawson

SPEC Incorporated, 3022 Sterling Circle, Suite 200, Boulder, Colorado, 80301, USA

Abstract. Recently, considerable attention has been focused on the issue of large ice particles shattering on the inlets and tips of cloud particle probes, which produces copious ice particles that can be mistakenly measured as real ice particles. Currently two approaches are being used to mitigate the problem: (1) Based on recent high-speed video in icing tunnels, probe tips have been designed that reduce the number of shattered particles that reach the probe sample volume, and (2) Post processing techniques such as image processing and using the arrival time of each individual particle. This paper focuses on exposing suspected errors in measurements of ice particle size distributions due to shattering, and evaluation of the two techniques used to reduce the errors. Data from 2D-S probes constitute the primary source of the investigation, however, when available comparisons with 2D-C and CIP measurements are also included. Korolev et al. (2010b) report results from a recent field campaign (AIIE) and conclude that modified probe tips are more effective than an arrival time algorithm when applied to 2D-C and CIP measurements. Analysis of 2D-S data from the AIIE and SPARTICUS field campaigns shows that modified probe tips significantly reduce the number of shattered particles, but that a particle arrival time algorithm is more effective than the probe tips designed to reduce shattering. A large dataset of 2D-S measurements with and without modified probe tips was not available from the AIEE and SPARTICUS field campaigns. Instead, measurements in regions with large ice particles are presented to show that shattering on the 2D-S with modified probe tips produces large quantities of small particles that are likely produced by shattering. Also, when an arrival time algorithm is applied to the 2D-S data, the results show that it is more effective than the modified probe tips in reducing the number of small (shattered) particles. Recent results

from SPARTICUS and MACPEX show that 2D-S ice particle concentration measurements are more consistent with physical arguments and numerical simulations than measurements with older cloud probes from previous field campaigns. The analysis techniques in this paper can also be used to estimate an upper bound for the effects of shattering. For example, the additional spurious concentration of small ice particles can be measured as a function of the mass concentration of large ice particles. The analysis provides estimates of upper bounds on the concentration of natural ice, and on the remaining concentration of shattered ice particles after application of the post-processing techniques. However, a comprehensive investigation of shattering is required to quantify effects that arise from the multiple degrees of freedom associated with this process, including different cloud environments, probe geometries, airspeed, angle of attack, particle size and type.

1 Introduction

Ice particles shattering on the inlets and tips of cloud particle probes produce small ice artifacts that can be erroneously included in measurements of ice particle size distributions. Artifacts produced from shattering of ice particles on optical cloud particle probes were reported in the literature over three decades ago (e.g., Cooper, 1978; Gardiner and Hallett, 1985). Cooper (1978) recognized the problem and introduced a method for removing shattered ice in post processing. Based on examination of two-dimensional images from the Particle Measuring Systems (PMS) model 2D-C probe (Knollenberg, 1970), he suggested that a burst of closely spaced particles, which is the typical pattern resulting from shattering, could be removed by comparison of individual particle arrival times. In simplistic terms, if ice particles are assumed to be randomly distributed in a cloud with concentration $< \sim 1\,\text{cm}^{-3}$, than particles with arrival times

equivalent to a spacing that is less than about 2 cm are considered artifacts, and are removed. Cooper (1978) introduced the arrival time approach, which was later refined by Field et al. (2003, 2006), Korolev and Isaac (2005) and Baker et al. (2009). The work presented by Baker et al. (2009) considers removal of splashing raindrops, which closely resembles shattered ice particles.

While the issue surrounding ice particles shattering on the inlets and tips of optical particle probes (hereafter referred to simply as "shattering") has been known since the 1970's, it has only been recently that the magnitude of the effect has been brought to the attention of the cloud physics community. Advances in high-speed digital videography and cloud particle probes have provided new insights into the shattering process. High-speed videography of ice particles shattering on probe tips in the Cox & Company Incoporated icing wind tunnel by the National Aeronautics and Space Administration (NASA) Glenn Research Center (GRC) and Environment Canada (EC) showed some remarkable results. Korolev et al. (2010a) shows digital videography of ice particles a few hundreds of micrometers in size shattering on probe tips, with small ice particles bouncing several mm upstream into the $100 \, \mathrm{m \, s^{-1}}$ airflow, and then traversing up to 3 cm across the airflow into the probe sample volume.

Advances in the electro-optics of linear-array cloud particle probes over the past four decades have provided new insights into measurements of cloud particle size distributions. To summarize, the 2D-C probe (Knollenberg, 1970) has 25-µm pixels with 32 photodiodes that are strobed at 5 MHz. The cloud imaging probe (CIP), designed and built by Droplet Measuring Technology (DMT) in the late 1990's (Baumgardner et al., 2001), has 64 photodiodes, 25-µm pixels and is strobed at 8 MHz. The 2D-S probe has 128 photodiodes, 10-µm pixels and is strobed at 20 Mhz. Lawson et al. (2006a) show laboratory results that demonstrate the ability of the 2D-S to image an 8-µm pixel fiber at speeds exceeding $200 \, \mathrm{m \, s^{-1}}$. In comparison, limitations of the time response of the photodiode array and front end amplifier in CIP and 2D-C probes may result in under sizing of small (e.g., $< \sim 100 \, \mathrm{µm}$) particles. Lawson et al. (2006a) showed measurements that suggest that the 2D-C does not image particles $< \sim 125 \, \mathrm{µm}$ at an airspeed of $103 \, \mathrm{m \, s^{-1}}$. Strapp et al. (2001) report on the efficiency of a 2D-C probe to detect 60-µm opaque circular dots on before a clear disk spinning at $100 \, \mathrm{m \, s^{-1}}$. The results show that the depth of field (DoF) of the 2D-C probe reduces from about 75 mm to 10 mm when the disk speed increases from 10 to $100 \, \mathrm{m \, s^{-1}}$, and that 80 % of the 60- µm spots are detected exactly at the center of the DoF, with the percentage of detected dots (including zero area images) decreasing to about 10 % within 3 mm of the center of DoF. Recent measurements show that a newer version of the CIP is capable of imaging 50- µm drops at $150 \, \mathrm{m \, s^{-1}}$, but that performance degrades at higher airspeeds (Lawson et al., 2010). These results suggest that the time response, and therefore the ability of the 2D-C and

CIP probes to image small particles, have improved over the past two decades. However, there is no evidence to date that shows that the 2D-C and CIP probes can detect particles less than 50 µm in size at jet aircraft speeds. On the other hand, the 2D-S probe has demonstrated the ability to image 10- µm particles at jet aircraft speeds.[1]

This paper is focused on exposing suspected errors in measurements of ice particle size distributions due to shattering, and evaluation of techniques used to reduce these errors. It is not intended to be a comparison of the relative performance of various imaging probes. However, Korolev et al. (2010b) recently evaluated shattering effects on 2D-C and CIP probes and reported that specially modified tips were more effective than an arrival time algorithm in reducing the effects of shattering. In this paper it is seen that, after evaluating limited data collected by two 2D-S probes, one with and one without modified tips, we find a different result; i.e., an arrival time algorithm is more effective in reducing the apparent effects of shattering than modified tips. The limited dataset with and without modified probe tips is not intended to provide guidance for quantitative assessment of shattering on the 2D-S probe. However, the data do show that, contrary to the results presented for 2D-C and CIP probes in Korolev et al. (2010b), the 2D-S probe with modified tips detects shattered particles in significant quantities. This may be due to the improved time response and size resolution of the 2D-S probe, or other factors, such as the probe tip design. Regardless, the results show that the arrival time algorithm is more effective than the modified probe tips in reducing the number of small (shattered) particles in these regions of large ice particles.

We concentrate on 2D-S measurements, which themselves contain uncertainties, some known and others that will likely be exposed over time. However, when available we have included comparable 2D-C and CIP measurements. A comparison of 2D-S and historical measurements also leads to implications regarding how uncertainties may impact cloud particle data in archives.

2   Comparison of measurements from a 2D-S and historical measurements

Historical aircraft measurements of ice particle size distributions using optical probes in deep stratus cloud systems, such as thick cirrus, have generally revealed a vertical profile

---

[1]The electronics in some 2D-C and CIP probes have recently been upgraded, so the results of the time-response comparisons now in the literature may not be applicable to all 2D-C and CIP probes. The time response and effective particle-size resolution of optical array probes is germane to the discussion of shattering presented in this paper, because reliable sizing of ice particles $< \sim 100 \, \mathrm{µm}$ could be critical to the ability to remove the effects of shattering in post processing.
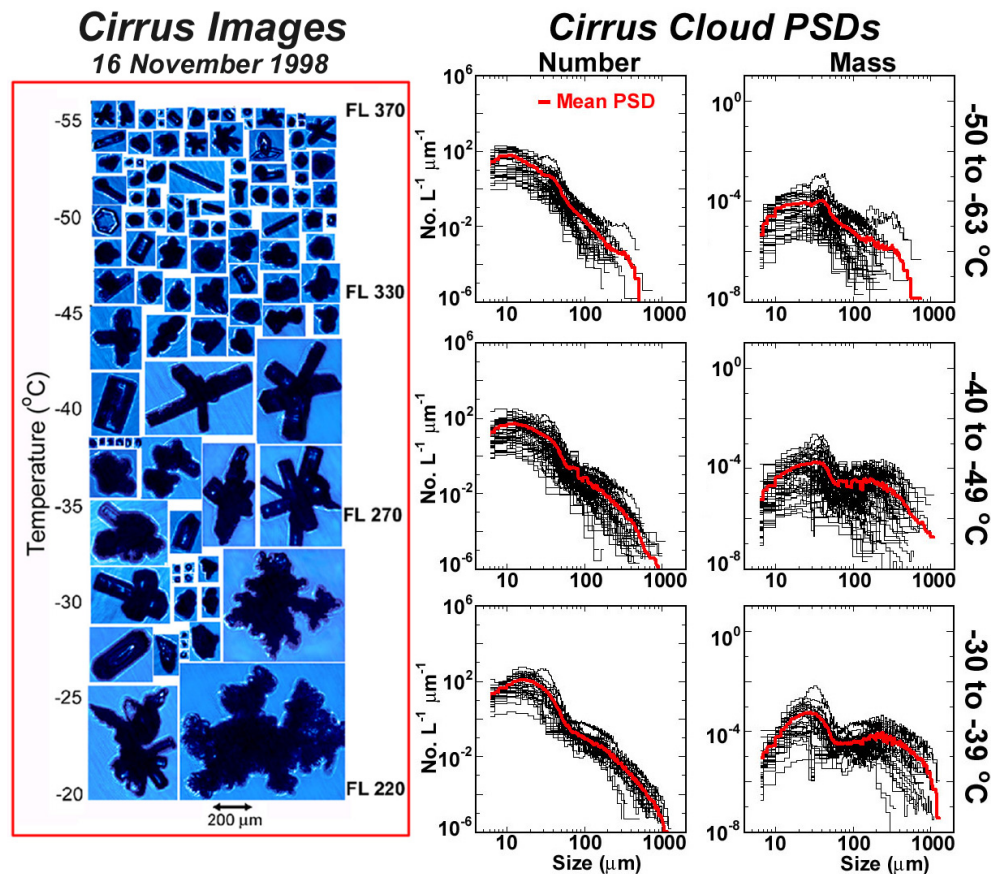
Fig. 1. Example of (left) vertical profile of CPI images in a deep orographically generated cirrus, and (middle and right panels) number and mass particle size distributions for three temperature ranges generated from 102 horizontal legs in cirrus, where average size distributions are shown in red. Small end of the size distributions are based on measurements from FSSP and large end from 2D-C probe, with CPI data scaled to fit in between. Adapted from Lawson et al. (2006b).

where small ice particles exist and typically dominate the size distribution throughout the depth of cloud (e.g., Lawson et al., 2006b). This is contrary to conventional thinking, which suggests that smaller particles will nucleate in higher concentrations at cold temperatures near cloud top and subsequently sublimate and disappear, grow via vapor diffusion, or aggregate into larger ice particles as they fall toward cloud base.

To help visualize the effects of shattering on archival data, we show two examples of vertical profiles of ice particle size distributions collected in relatively deep cirrus clouds. The first example shows average ice particle size distributions using older cloud particle probes that are believed to be subject to errors from shattering. The second example shows data from the 2D-S probe, which used modified probe tips based on the Korolev design technique and particle arrival times (Baker et al. 2009) to remove shattered ice in post processing. Figure 1 shows an example from Lawson et al. (2006b) of particle size distributions and number concentrations based on multiple penetrations of cirrus clouds. Composite size distributions were put together using

measurements from a forward scattering spectrometer probe (FSSP), a cloud particle imager (CPI) and a 2D-C probe. The FSSP was used to establish the small particle end of the size distribution (generally less than about 30 μm) and the 2D-C established the large end. CPI data were scaled to merge with the FSSP and 2D-C measurements (see Lawson et al., 2006b for details).

A combination of gravity waves and homogenous nucleation at these cold temperatures is a possible theoretical explanation for the relatively high $(846 \, l^{-1})$ average ice concentration near cloud top in Fig. 1 (Kärcher and Ström, 2003; Jensen et al., 2009). Some investigators have reported even higher $(>1 \, cm^{-3})$ ice concentrations in regions where the maximum particle size is about 100 μm (Gayet et al., 2002; Kärcher and Ström, 2003; Lawson et al., 2006b). Shattering is not thought to be a major contributor to ice concentration in this situation. However, the high $(2.17 \, cm^{-3})$ average ice concentration near cloud base in Fig. 1 cannot be explained theoretically.

Using particle arrival times from a fast FSSP, Field et al. (2003) shed light on this issue when they showed that

the FSSP was very sensitive to shattering, and that the shattered artifacts could significantly increase the small particle concentration. Most of the measurements that suggest high concentrations of small ice in regions with large ice (i.e., > a few hundreds of microns) have been reported using (or in the case of the CPI scaled by) a scattering probe such as the FSSP (e.g., Fig. 1).

In contrast to the vertical distribution of small ice particles seen in Fig. 1, the measurements in Fig. 2 were collected using a 2D-S probe in a deep cirrus cloud investigated from 19:36:30–19:59:00 UTC on 10 February 2010 during the Small PARTIcles in CirrUS (SPARTICUS) project. This example was chosen from the SPARTICUS dataset because it shows high ($2.7\,cm^{-3}$) concentrations of small ice near cloud top (and the CPI images reveal nearly all small ice), but only $44\,l^{-1}$ near cloud base, including bullet rosettes with sizes of hundreds of microns. A comparison of the size distributions in Figs. 1 and 2 shows that both the concentration and mass distributions have similar shapes near cloud top where there were few large ice particles. However, lower in the cloud where there are higher concentrations of large ice particles, the mode of the mass distribution in Fig. 1 peaks between 10 and $100\,\mu m$, whereas the mass mode peaks between 100 and $500\,\mu m$ in Fig. 2. The much smaller mass mode in Fig. 1 is most likely due to particle shattering on the inlet of the FSSP used in these studies. Jensen et al. (2009) show that the shattering on scattering probes with inlets like the FSSP has a significant effect on the second moment (i.e., extinction) of the cloud particle size distribution. Errors from shattering that have affected measurements of extinction coefficient suggest that significant errors could occur in radiative transfer models and remote retrievals.

3 Performance of tip modifications and arrival time algorithms in field campaigns

3.1 SPARTICUS field campaign

During the SPARTICUS project the SPEC Learjet was flown on a special mission with two 2D-S probes; one probe with "unmodified" ("standard") tips and one probe with tips "modified" using the Korolev design technique. Korolev developed probe tips to reduce shattering based on theoretical considerations and high-speed video in the Cox & Company icing tunnel. The process was iterative and the design of (2D-C and CIP) probe tips evolved over time. Korolev eventually patented the probe tip design used on the 2D-C and CIP probes.[2]

---

[2] Korolev, A., *Probe Tips for Airborne Instruments Used to Measure Cloud Microphysical Parameters*, United States Patent No. 7 861 584, Issued: 4 January 2011, Owner: Her Majesty the Queen in Right of Canada, as Represented by The Minister of Environment.
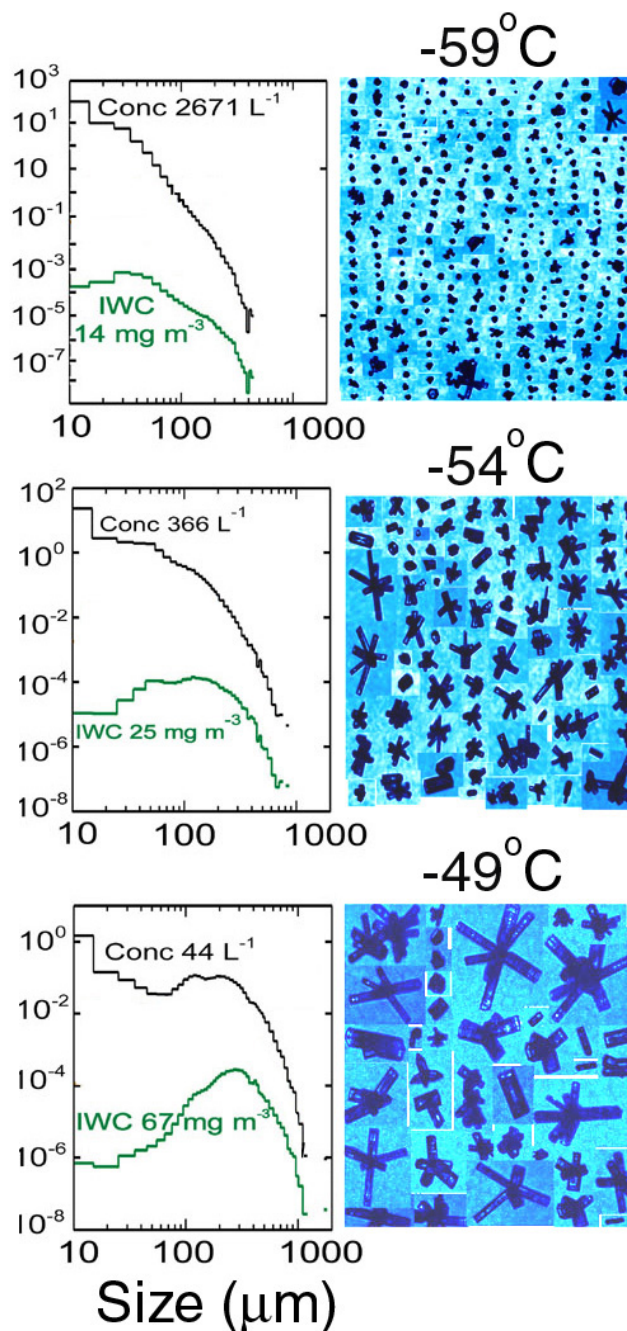

Fig. 2. Example from the SPARTICUS project showing (left) concentration and mass particle size distributions derived from the 2D-S and (right) images from the CPI.

Lessons learned from the high-speed video revealed some fundamental concepts regarding the shattering process that Korolev communicated to SPEC engineers. The 2D-S probe that is termed the "standard" or "unmodified" probe in this paper had tips that were designed by SPEC to minimize shattering, but without benefit of information later provided by Korolev. The 2D-S with "modified" probe tips was designed

Fig. 3. Photograph showing the SPEC Learjet used in the SPARTI-CUS project with two 2D-S probes, one with tips modified to reduce shattering, and the other with standard tips.

Fig. 4. 2D-S size distributions from Learjet penetration (20:54:08 to 20:54:21 UTC, 23 July 2010) of a small cumulus cloud containing only water drops. The light green trace is from the probe with standard tips and includes shattered particles. A dark green trace is from the probe with standard tips after applying the shattering algorithm, but is not visible behind the light green trace. The red trace is from the probe with modified tips and includes shattered particles. A blue trace from the probe with modified tips after applying the shattering algorithm is barely visible near the red trace.

and fabricated based on information that Korolev delivered in person to SPEC engineers. Appendix C shows photographs and drawings of 2D-S probe tips that are germane to this paper. As shown in Fig. 3, the "standard" and "modified" 2D-S probes were about 1.5 m apart and were identical except for the probe tips. However, it is always important to keep in mind that even though two particle imaging probes are constructed to be identical, their comparative performance is rarely identical (e.g., Gayet et al., 1993).

On 23 July 2010 the Learjet penetrated a cloud region with only small cloud drops, where no shattering is expected, and a region of precipitation with large ice aggregates, where shattering is expected. Figure 4 shows average 2D-S drop size distributions in the region with only small cloud drops, with and without application of the shattering algorithm, for both 2D-S probes shown in Fig. 3. There is reasonably good agreement between the two probes in the cloud with only small drops where no shattering is expected, and application of the shattering algorithm had a negligible effect on the drop size distributions. This demonstrates that on this mission both probes recorded similar concentrations of small particles when there were no shattering effects. Later in the mission, the Learjet penetrated near the base of a thunderstorm anvil that contained a wide range of ice particle sizes, extending out to a few millimeters. This 3-min segment was selected because it was the only period with millimeter-size precipitating ice that the Learjet encountered on this mission. Figure 5 shows examples of typical images from both probes, i.e., with unmodified and with modified probe tips. Figure 6 shows a comparison of particle size distributions from the two 2D-S probes, with and without modified tips; and with and without application of the arrival time shattering removal algorithm. Figure 6 shows that all of the size distributions
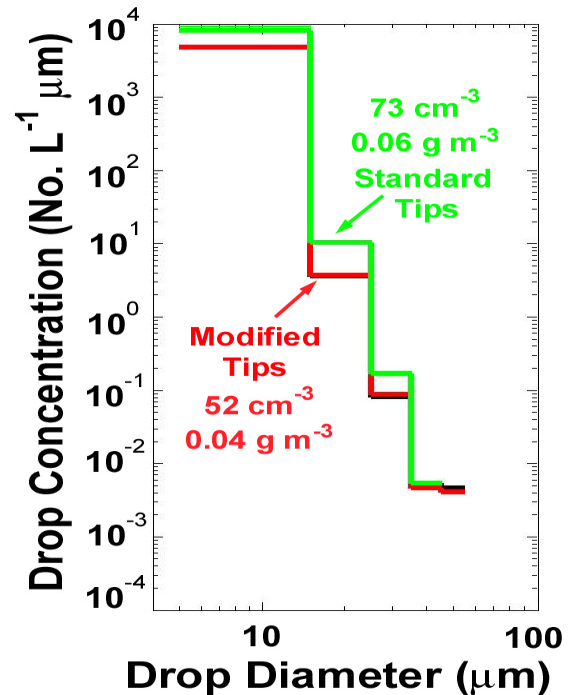
tend to converge at particle sizes larger than about 200 µm, which suggests that (in this case) the erroneous effects of shattering are less apparent in the larger portion of the size distribution. [3]

The images in Fig. 5 suggest, and the size distributions in Fig. 6 support the premise that the modified probe tips significantly reduce, but do not eliminate shattering. During the penetration of precipitating dendrites, post processing of the 2D-S probe with standard tips identified 153 out of 507 (30 %) of the images >1 mm as shattered images. In comparison, the modified probe tips eliminated more than half this amount, with 54 out of 450 (12 %) of the images >1 mm being identified as shattered images.

---

[3] Note that each 2D-S probe used in this study actually contains two independent probes, so that it is possible to compare four 2D-S probe measurements in this study. For the sake of clarity in presenting 2D-S data in this paper, the two (H and V) channels of each probe were averaged, and only regions where the two channels were in good agreement were used, avoiding any regions where obvious instrumentation effects adversely influenced the measurements.
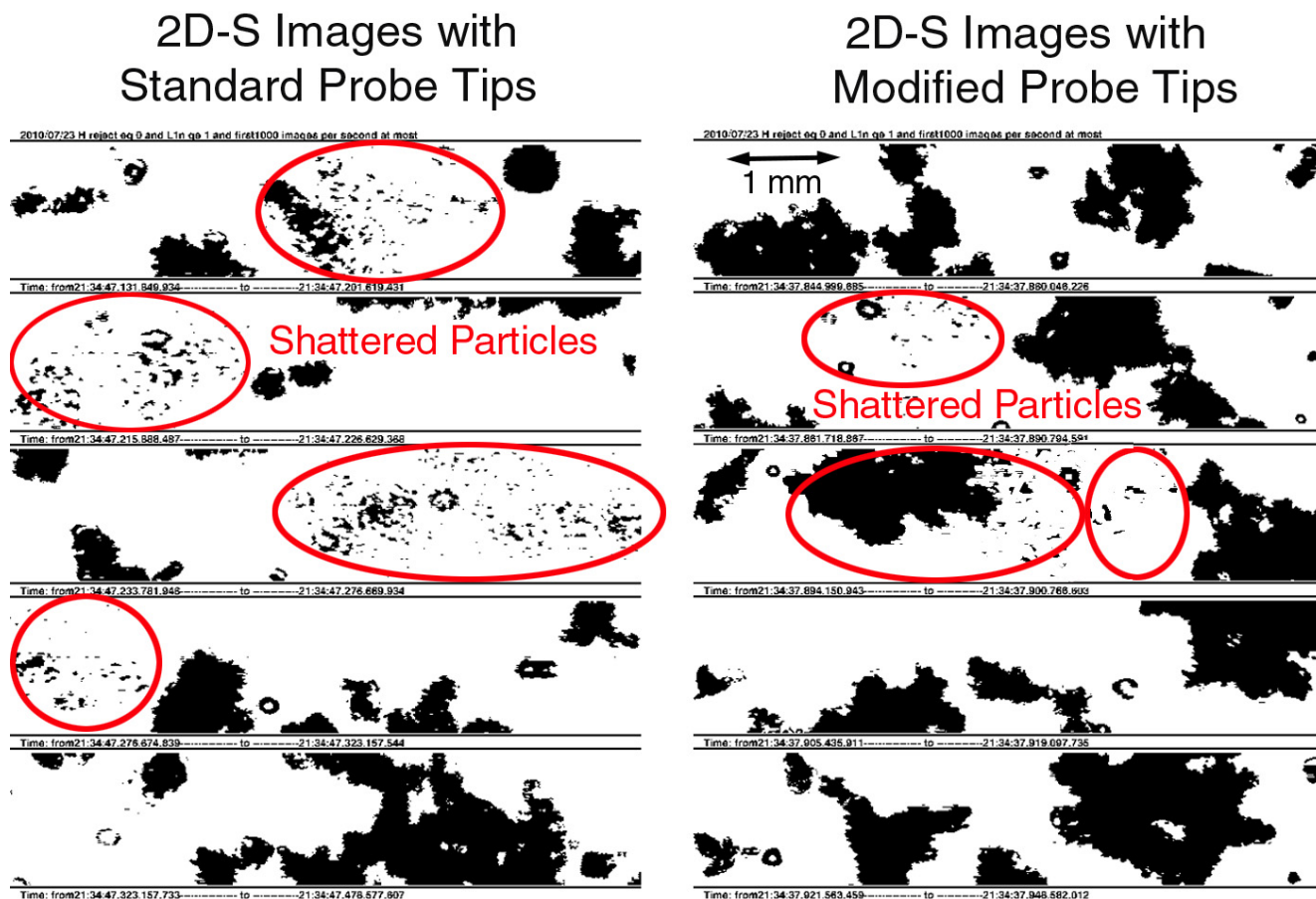
2D-S Images with Standard Probe Tips

2D-S Images with Modified Probe Tips

Fig. 5. Examples of 2D-S images from two 2D-S probes flown side-by-side on the SPEC Learjet (Fig. 3) during the SPARTICUS project, one probe had standard 2D-S probe tips (left) and (right) the other with tips modified to reduce the effects of shattering.

Figure 6 shows that the size distribution with the unmodified probe tips and without application of the arrival time removal algorithm (green trace) contains the most particles with sizes $<200\,\mu$m. The size distribution with modified probe tips and without application of the arrival time removal algorithm (red trace) contains the second most particles with sizes $<200\,\mu$m, which also shows that the probe with modified probe tips is effective in reducing shattering. However, the two size distributions that have been processed using the arrival time algorithm to remove shattered particles contain far fewer particles $<200\,\mu$m than either of the other size distributions, regardless whether the probe has modified tips, or not. Thus, in this case, the arrival time algorithm is more effective than the modified probe tips in reducing the effects of shattering on these 2D-S probes.

The average bulk parameters, total number concentration (N), extinction coefficient (β_{ext}) and ice water content (IWC) are also shown in Fig. 6. In this example, without application of the arrival time algorithm the modified tips make a significant difference in N ($707\,l^{-1}$ vs. $214\,l^{-1}$). Application of the arrival time algorithm reduces N from $707\,l^{-1}$ to $37\,l^{-1}$ with the standard tips and from $214\,l^{-1}$ to $50\,l^{-1}$ with the modified tips. Thus, the modified tips reduce N by $493\,l^{-1}$ and application of the arrival time algorithm reduces N by only an additional $177\,l^{-1}$. On the other hand, without application of the arrival time algorithm the modified tips make no difference in β_{ext} and only 3 mg difference in IWC. When the arrival algorithm is used in the computation of β_{ext} and IWC, the differences are much larger. Application of the arrival time algorithm reduces β_{ext} from $2.5\,km^{-1}$ to $2.0\,km^{-1}$ with the standard tips, and from $2.5\,km^{-1}$ to $2.2\,km^{-1}$ with the modified tips. The arrival time algorithm reduces IWC from $100\,mg\,m^{-3}$ to $84\,mg\,m^{-3}$ with the standard tips, and from $103\,mg\,m^{-3}$ to $90\,mg\,m^{-3}$ with the modified tips. Thus, in this example application of the arrival time algorithm makes a much more significant impact on the second and third moments of the size distribution than does the modified tips.

Another method for examining the effects of shattering is to generate a scatter plot of the concentration of small (shattered) particles versus the mass of large (shattering) particles (Jensen et al., 2009). In this way, it is possible to see if the concentration of smaller particles that may (or may not)
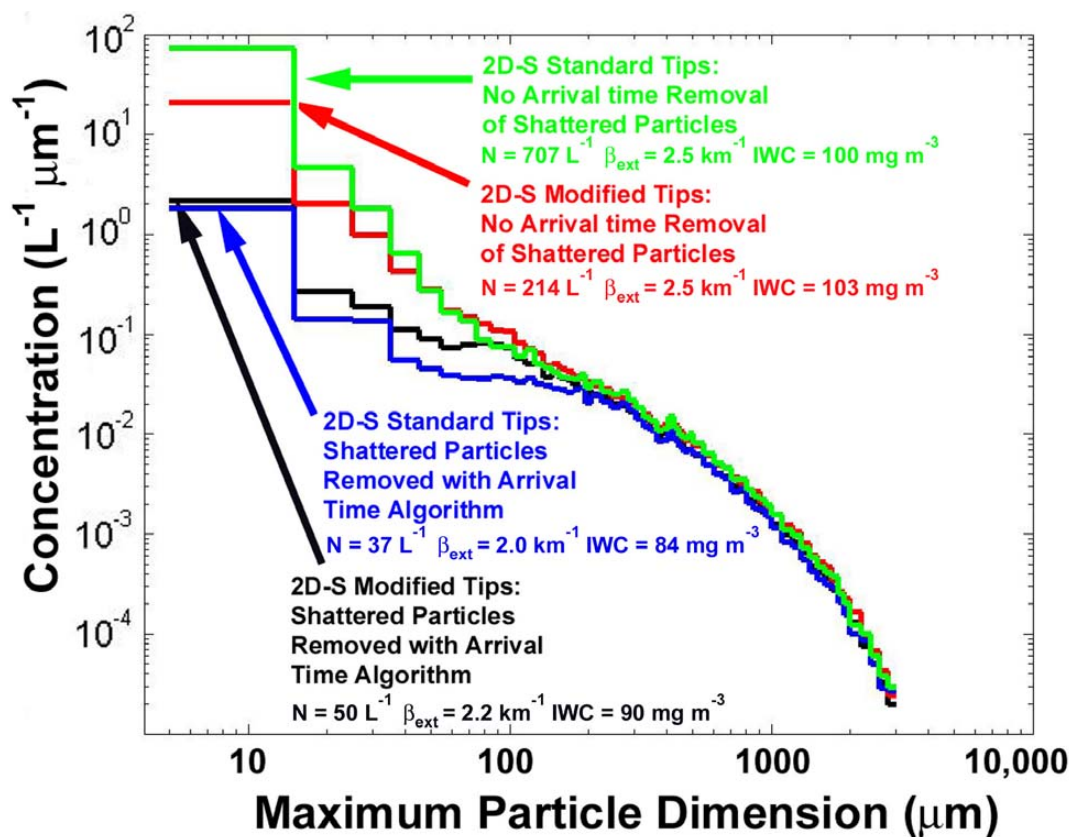
Fig. 6. Average particle size distributions derived from 2D-S measurements collected in large ice aggregates from 21:34:18–21:37:16 UTC, 23 July 2010. Data are from two 2D-S probes installed side-by-side on the SPEC Learjet (Figs. 3–5). One probe had standard probe tips and the other probe was equipped with probe tips modified to reduce shattering. Size distributions are shown with and without the effects of an arrival time algorithm to remove shattering. Total particle concentration (N), extinction coefficient (β_{ext}) and ice water content (IWC) were derived from each average size distribution.

have been generated from shattering, are correlated with increasing mass of large particles, which are responsible for generating shattered particles. Figure 7 shows 1-Hz scatter plots of 2D-S data with standard tips and with modified tips from the 21:34:18–21:37:16 UTC, 23 July 2010 SPARTICUS anvil penetration discussed above. As seen in Fig. 7a, the scatter plot with the standard tips shows a very strong correlation between the concentration of small particles and increasing ice water content without application of the arrival time algorithm. After application of the arrival time algorithm there is still a correlation, but the magnitude of the trend is considerably less. Figure 7b shows that the modified tips reduces the number of small (shattered) particles, but the correlation between the concentration of small particles and increasing ice water content is still strong. Application of the arrival time algorithm reduces the shattering trends in Fig. 7a and b to about the same magnitude, regardless whether the probe has standard or modified tips. The data in Fig. 7 suggests that, in this case, the arrival time algorithm produces approximately the same result, regardless of whether the 2D-S probe has standard or modified tips. The data also suggest that using the 2D-S probe with modified tips alone is not sufficient to reduce shattering to the level achieved after the arrival time algorithm is applied.

The scatter plots in Fig. 7 can also be interpreted to provide an estimate of the effectiveness of removing small ice particles due to shattering, or alternatively, an estimate of the maximum number of natural small ice particles. For example, the data in Fig. 7 show that for this particular case, for the unmodified tips, approximately $8500 \, \mathrm{l}^{-1}$ of (spurious) small ice particles are produced for each $\mathrm{g\,m^{-3}}$ of large ice. Similarly, measurements from the probe with the modified tips show that about $2000 \, \mathrm{l}^{-1}$ small ice particles are produced for each $\mathrm{g\,m^{-3}}$ of large ice. Since both probes yield about the same result after application of the arrival time algorithm, it is tempting (and possible) that the remaining $\sim 350 \, \mathrm{l}^{-1}$ per $\mathrm{g\,m^{-3}}$ are real ice particles, naturally correlated with large ice mass content. However, it is also possible that these ice particles are still spurious events not removed by the tips and algorithm, i.e., there are no small ice particles in this region of precipitating aggregates. If this is the situation, then these data provide an estimate of the remaining spurious effects of
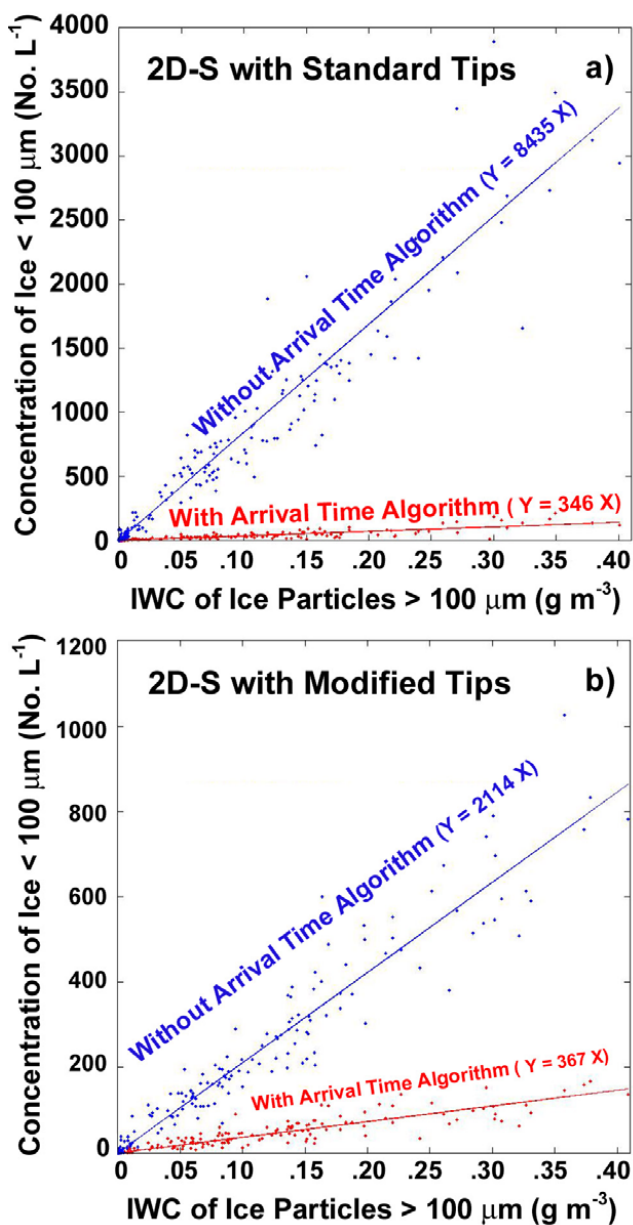
Fig. 7. Scatter plots of the concentration versus ice water content of ice particles $<100\,\mu m$. Data collected in large ice aggregates with two 2D-S probes installed side-by-side on the SPEC Learjet (Figs. 3–6). One probe **(a)** had standard probe tips and the other probe **(b)** was equipped with probe tips modified to reduce shattering. Effect of the arrival time algorithm to remove shattering is shown on each plot.

shattering, i.e, in this case $\sim 350\,l^{-1}$ of small ice particles per $g\,m^{-3}$ of large ice remain after shattering prevention with modified tips and removal with the arrival time algorithm. Since it is not possible to know the actual concentration of small ice particles, in this case: (1) $350\,l^{-1}$ per $g\,m^{-3}$ is an estimate of the upper bound of the possible remaining effects of shattering, or (2) an upper bound of the natural ice concentration in the cloud.

The measurements shown in Figs. 6 and 7 suggest that the modified tips reduce the number of small (shattered) particles, but not as effectively as the arrival time algorithm. Also, there is still a trend for increasing small particles with increasing ice water content, even with modified tips and application of the arrival time algorithm. This can be explained either by a process that is actually generating small particles when there are more large ice particles (e.g., particle-particle collisions), or that not all of the shattered particles are being removed by the modified tips and arrival time algorithm. We would like to point out a scenario where a shattered particle can be counted as a natural ice particle. If only one shattered small particle passes through the sample volume (i.e., the remainder of the shattered small particles are out of the depth of field), the one small particle in the depth of field will be not be rejected by the arrival time algorithm and will be counted as a natural ice particle (Korolev et al., 2010a). Since the depth of field of imaging probes is very small for small particles, the effective particle concentration is increased dramatically. The probability of this occurring is unknown at this time and would require a dedicated investigation, perhaps requiring high-speed video of shattered particles in various airborne flight and cloud conditions. However, the methodology presented here (i.e., Fig. 7 and associated discussion) is a method for estimating the maximum contribution from shattering.

After examining the data in Fig. 7, it is tempting here to state that shattering may have artificially increased the concentration of small particles by an order of magnitude. However, it is important to keep in mind that the contribution from shattering is relative to the natural concentration of small particles. If the contribution from shattering of very large particles in the example in Fig. 7 was hypothetically added to the concentration of natural small particles at the top of the cirrus cloud example in Fig. 2, then the contribution from shattering would add $<10\,\%$ to the total particle concentration. For this reason, we recommend reporting quantified *additive* effects and to avoid reporting *multiplicative* values.

3.2 AIIE field campaign

The Airborne Icing Instrumentation Evaluation (AIIE) field campaign was conducted near Ottawa in March–April 2009 (Korolev et al., 2010b). Data were collected with the National Research Council (NRC) of Canada Convair 580 research aircraft in deep precipitating glaciated cloud systems associated with frontal clouds. There was only one 2D-S probe available, so the probe was flown on one research flight without the modified tips, and then on another flight with the modified tips. Figure 8 is reproduced from Fig. 5 in Korolev et al. (2010b), with the addition of 2D-S measurements from the same time period. The data in Fig. 8a show that, contrary to 2D-S data shown in Fig. 7, modified 2D-C tips are more effective in removing small (shattered) particles than is the
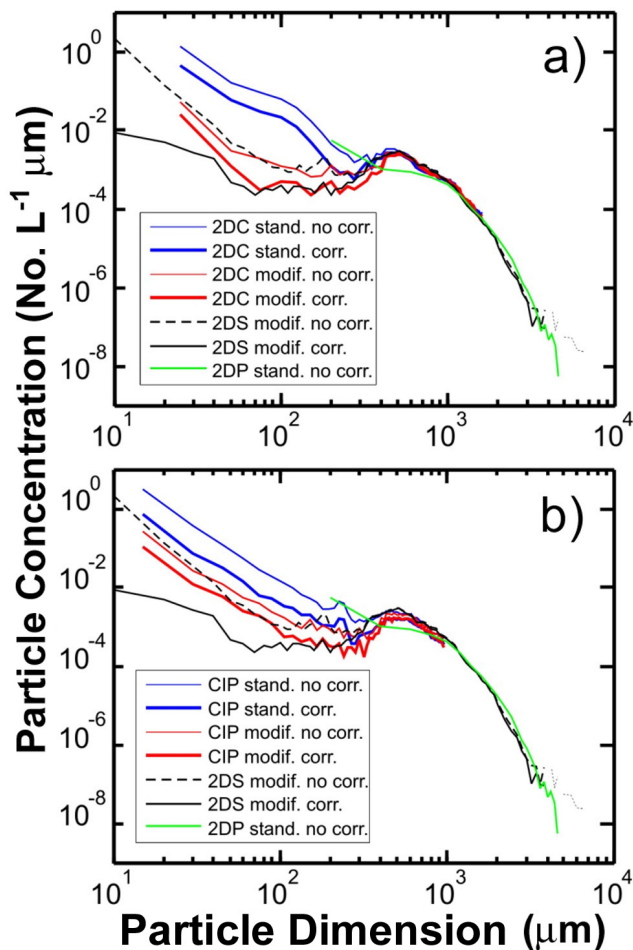
Fig. 8. Particle size distributions from 14:09:00–14:21:00 UTC, 8 April 2009, collected during the AIIE field project. Data are reproduced from Korolev et al. (2010b) with the addition of 2D-S data for the same time period. "stand." Means standard probe tips; "modif." means modified probe tips, "corr." means data have been adjusted using an arrival time algorithm and "no corr." means that no arrival time algorithm has been applied.

arrival time algorithm (indicated by "corr." in the figure)[4]. The CIP data in Fig. 8b shows the same trend as the 2D-C in Fig. 8a. In Fig. 8a and b, 2D-S data without ("no corr.") and with ("corr.") arrival time corrections are shown with modified probe tips. A comparison of all data in Fig. 8 suggest that the 2D-S probe with application of arrival time correction removes the most small (shattered) particles. The 2D-C probe with arrival time correction is closest to the 2D-S PSD, with the CIP probe showing the most deviation from the 2D-S results.

Figure 9 shows 2D-S measurements from data collected during the AIIE field program on two different flights in similar cloud conditions; one flight when the probe was flown

---
[4] The particle arrival time algorithm applied to the AIIE data was developed and applied by Alexei Korolev.

without modified probe tips, and the second flight with modified tips. Each data point in Fig. 9 represents a 15 to 30 s average calculated in the following way. One-hertz data 2D-S are screened for periods when the large ($>55\,\mu m$) particle concentration exceeds $1\,m^{-3}$ for a minimum of 15 s. During this period the 1-Hz median volume diameter must remain between 0.8 and 1.2 of its mean and the large particle concentration must remain between 0.4 and 2.0 of its mean. If an accepted time period exceeds 30 s the first 15 s are cut off as a separate period and the algorithm continues. So all accepted periods are between 15 and 30 s in duration. 2D-S data from the flights with and without the modified tips were processed with and without application of the arrival time algorithm, producing the four scatter plots seen in Fig. 9. The data in Fig. 9 show that without applying the arrival time algorithm, the concentration of small ($<55\,\mu m$) ice particles is about $6000\,l^{-1}$ per $g\,m^{-3}$ with the unmodified tips, compared with about $1000\,l^{-1}$ per $g\,m^{-3}$ with the modified tips. However, there is still a strong correlation between increasing concentration of small particles and ice water content, until the application of the arrival time algorithm. Once the arrival time algorithm is applied the average concentration of small ice particles is about $20\,l^{-1}$ per $g\,m^{-3}$ with both the unmodified and modified tips, and there is no correlation between increasing small ice particles and ice water content.

The data in Fig. 9 suggest that, for the 2D-S probe in these cloud conditions, the modified tips reduce, but do not eliminate the trend of increasing small particles with increasing ice water content. On the other hand, the data in Fig. 9 do show that, in this case, the arrival time algorithm eliminates the correlation between large and small (shattered) particles. It should be pointed out, however, that because there is no way of knowing the actual concentration of small particles (i.e., there could be none), this does not imply that the arrival time algorithm eliminates all of the shattered particles. As in Fig. 7, though, an estimate of the upper bound on the amount of shattered ice particles and natural ice particles can be derived from these scatter plots. The results shown in Figs. 7 and 9 are only two examples, and shattering is likely to depend on many factors, including ice crystal size, type, airspeed, angle of attack and temperature, to mention some of the more important factors. For example, the data in Fig. 7 still show a (weak) correlation between large and small particles in the large particle region of an anvil cloud, even with modified tips and application of the arrival time algorithm.

3.3 ISDAC field campaign

The 2D-S, 2D-C and CIP probes were also flown together in April 2008 on the NRC Convair 580 research aircraft during the Department of Energy (DOE) Atmospheric Radiation Measurement (ARM) Indirect and Semi-Direct Aerosol Campaign (ISDAC). Figure 10 shows typical particle images and size distributions from several particle probes that were flown together below the base of a precipitating Arctic
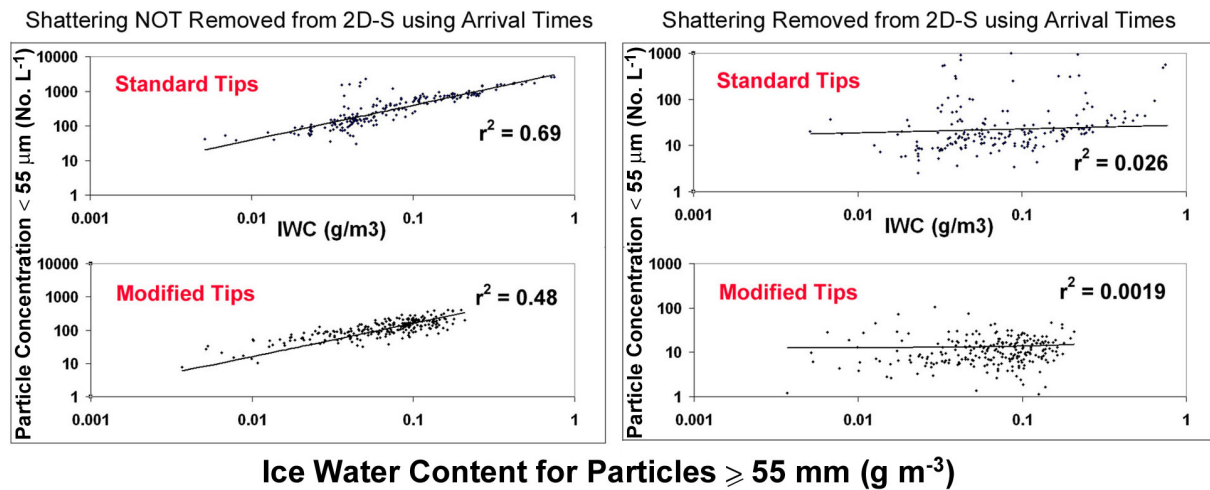
Fig. 9. Scatter plots of the concentration of ice particles ($<55\,\mu m$) versus ice water content $=>55\,\mu m$. Data were collected during the AIIE field project with a 2D-S probe installed on the NRC Convair 580. Data were collected with standard tips from 17:54:53–20:16:44 UTC, 1 April 2009. Data were collected with modified tips from 14:32:32–16:24:37 UTC, 4 April 2009. The 2D-S probe was flown with standard tips on one flight (top two panels), then with modified tips in similar conditions on a second flight (bottom two panels). Effect of the arrival time algorithm to remove shattering is shown on plots on the right side.

stratus cloud investigated from 01:20:00 to 01:26:40 UTC, 26 April 2008. The instrument acronyms shown on the figures and their affiliations are listed in the figure caption. Figure 11 shows typical particle images and size distributions from the same instruments flown in the mixed-phase region 300 m above the base of the same Arctic stratus cloud from 02:48:40 to 02:48:53 UTC. Only the 2D-C had probe tips with an aggressive design to reduce shattering. However, the 2D-S probe did have tips that were designed to reduce shattering, based on understanding of ice particle shattering at that time.

The lower left sides of Figs. 10 and 11 show size distributions without removing shattered particles, while the right sides show the same time periods using an arrival time algorithm to remove shattered (i.e., closely spaced) particles on the SPEC 2D-S and fast FSSP, the EC 2D-C and the DMT CIP.[5] The size distributions without application of the arrival time algorithm are all in reasonably good agreement, both below cloud base in precipitating dendrites (where small particles are not thought to be abundant), and in the mixed-phase region where the CDP and FSSP probes show about $80\,cm^{-3}$. In the precipitating dendrite size distributions (Fig. 10), the SPEC fast FSSP and 2D-S probes show a significant reduction in the concentration of small particles with the arrival time algorithm applied. The particle concentration in the size range from 5 to $300\,\mu m$ is reduced from about 20 to 21^{-1}. The 2D-C, which has a 25-μm pixel size, also shows a reduction in particle concentration of about 3 to 0.31^{-1} in the 25 to $300\,\mu m$ size range. On the other hand, there is very lit-

tle change in the CIP size distribution and the small particle concentration actually increases in the smallest bins (due to re-sizing of some of the larger donut-shaped particles). In this case the application of an arrival time algorithm has a result similar to the AIIE results shown in Fig. 8, where both the 2D-S and 2D-C size distributions show significant reductions in small particles, whereas the CIP shows much less of an effect.

In the mixed-phase region of the same cloud (Fig. 11), the natural small particle (i.e., cloud drop) concentration is about $80\,cm^{-3}$, which is much higher than below cloud base. Even though the concentration of large particles in the mixed-phase is about the same as in the precipitation below cloud base, the total particle concentration is not significantly affected when the arrival time algorithm is applied. The most significant difference when the arrival time algorithm is applied is seen in the region from about 50 to $150\,\mu m$, but the percentage change is still quite small. When shattered particles are removed particle concentration in the 50 to $150\,\mu m$ size range changes from 1.4 to 0.41^{-1}, extinction coefficient goes from 0.08 to $0.05\,km^{-1}$ and ice water content changes from 7 to $5\,mg\,m^{-3}$. The percentage change in small (cloud drop) particles when shattered particles are removed is negligible. Particle concentration changes from 66 304 to $66\,2951^{-1}$, extinction coefficient goes from 10.78 to $10.76\,km^{-1}$ and liquid water content changes from 40.3 to $40.0\,mg\,m^{-3}$. A comparison of Figs. 10 and 11 emphasizes the reason why shattering should be reported as an additive effect and not a multiplicative effect. Jensen et al. (2009) show a result similar to Figs. 10 and 11 for low and high concentrations of natural small ice at the top of an aged tropical anvil cloud; i.e., shattering with low natural ice

_____

[5]2D-C and CIP arrival time algorithm developed and applied by Greg McFarquhar's group at the University of Illinois.
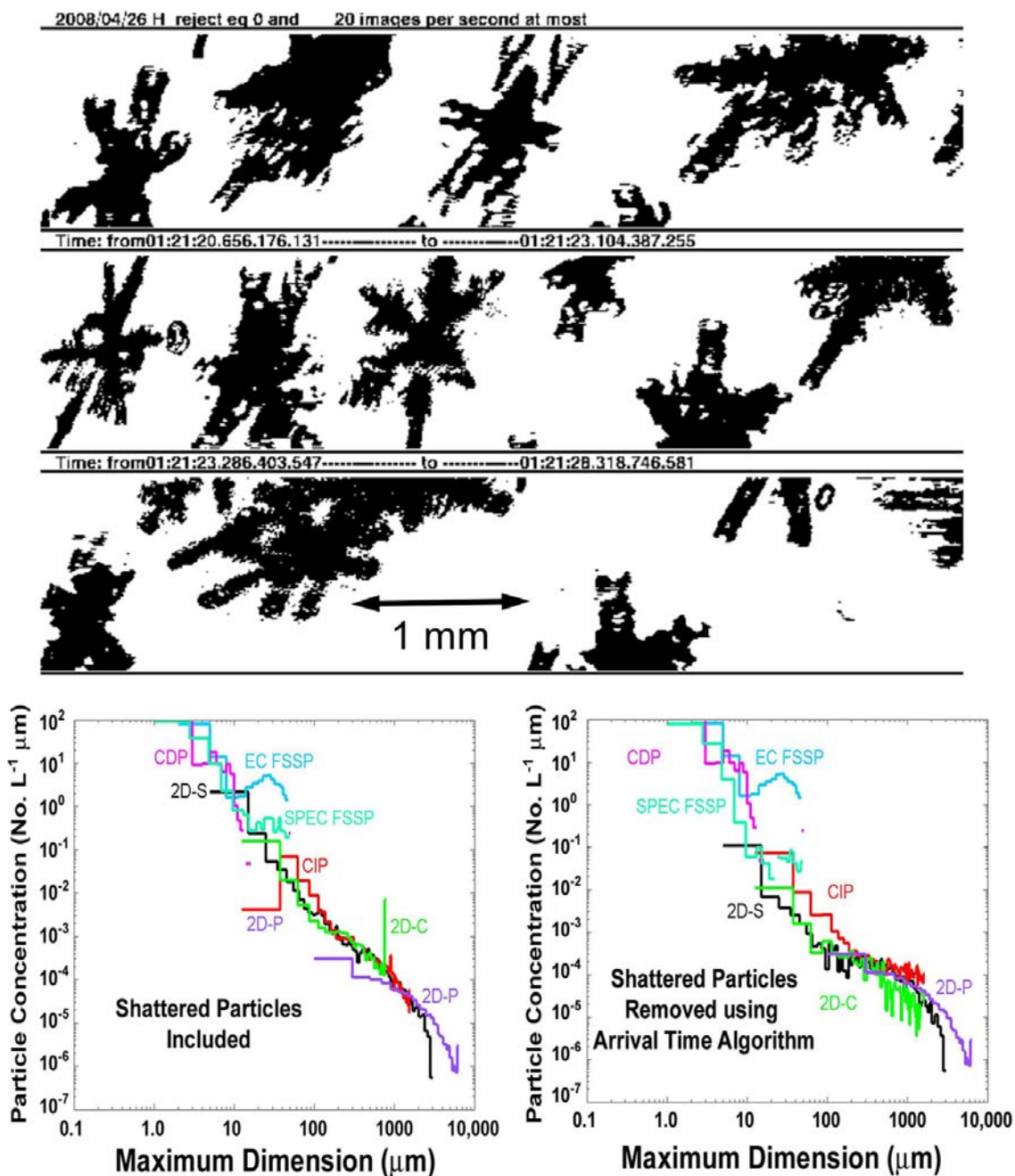
Fig. 10. (top) 2D-S Images and (bottom) particle size distributions from several cloud particle probes flown on the Canadian Convair 580 in precipitating dendrites below cloud base during ISDAC from 01:20:00 to 01:26:40 UTC, 26 April 2008. Left panel shows measurements with shattered particles included and right panel with shattered particles removed using arrival time algorithm. EC FSSP = Environment Canada FSSP. CDP = DMT CDP. SPEC FSSP = SPEC Fast FSSP. CIP = DMT CIP. 2DC = EC 2DC. 2DP = EC.

makes a significant contribution to total particle concentration, whereas this is not the case when the natural ice concentration is high.

3.4 MACPEX field campaign

Figure 12 shows another example of 2D-S measurements from a very recent field campaign, the Mid-latitude Airborne Cirrus Properties Experiment (MACPEX). The measurements are consistent with numerical models of cirrus and cirrus anvils, which are formulated on basic physics that lend
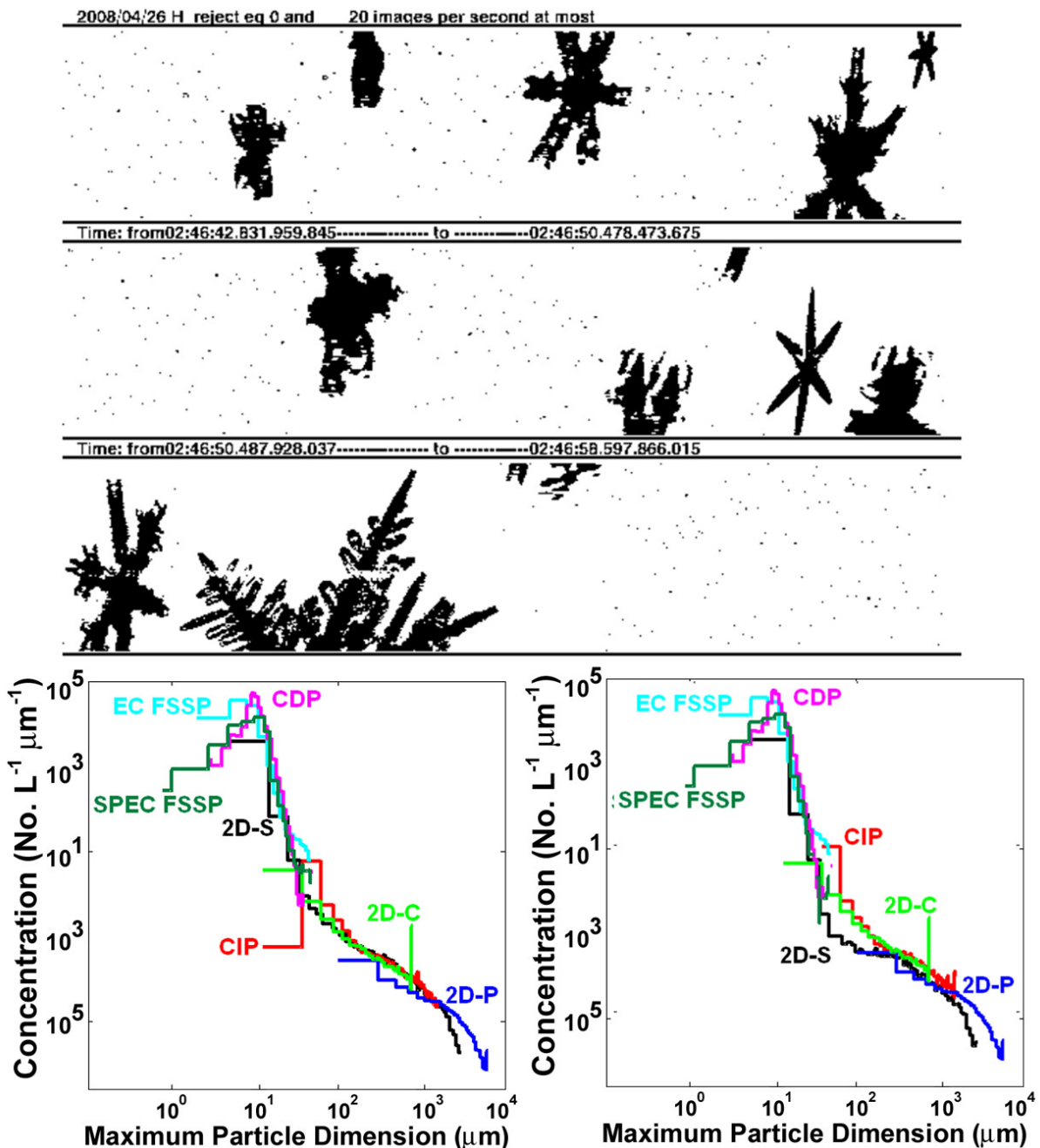
Fig. 11. As in Fig. 10, except data were collected in the mixed-phase region of the same Arctic cloud from 02:48:40 to 02:48:53 UTC, 26 April 2008.

physical credibility to the very large differences in 2D-S particle concentrations observed in the two regimes. The high particle concentration in the anvil cirrus is the result of homogeneous freezing of drops in convective updrafts and subsequent outflow in the anvil. Fridlind et al. (2004) show that model simulations produce in excess of $10\,cm^{-3}$ of ice particles in the convective outflow regions of anvils. On the other hand, Comstock et al. (2008) show numerical simulations of synoptic cirrus with typical concentrations of 1 to $100\,l^{-1}$. Consistent with simple physical arguments and numerical simulations, Fig. 12 shows relatively low $(11\,l^{-1})$ concentrations of small particles in cirrus that was generated synoptically, and much higher $(2059\,l^{-1})$ concentrations of small particles in anvil cirrus, located several km downwind of convection. Note that unlike Figs. 1 and 2, the ordinate in Fig. 3 is dN/dlogD, which tends to emphasize the reduction of small particles in the plot.
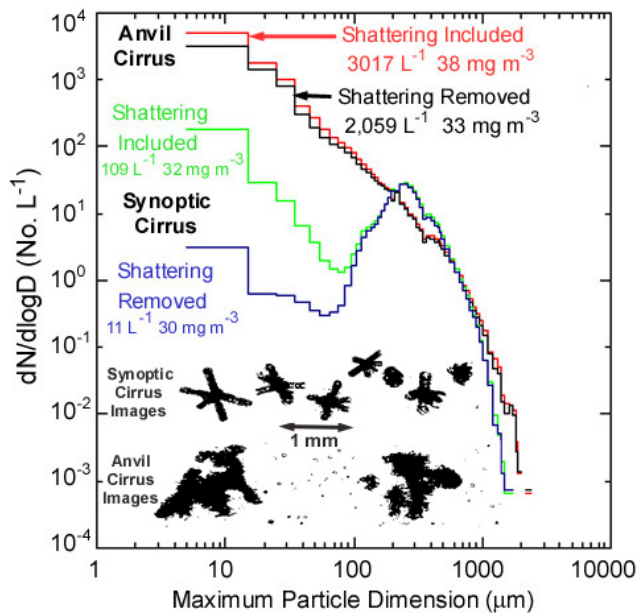
Fig. 12. Particle size distributions as a function of concentration from 2D-S probe measurements in anvil and synoptic cirrus sampled on 14 April 2011 from 18:36:00–18:51:00 UTC (synoptic cirrus), and 11 April 2011 from 17:37:50–18:46:10 UTC (anvil cirrus) by the NASA WB-57 during the MACPEX field campaign. Example 2D-S images from each time period are shown below the size distributions.

Fig. 13. As in Fig. 12 except the size distributions are shown as a function of particle mass.

The data in Fig. 12 are also a good example of how quoting multiplicative shattering factors can be very misleading. The shattering algorithm reduces the total number concentration in the synoptic cirrus by an order of magnitude (i.e., from $109\,\mathrm{l}^{-1}$ to $11\,\mathrm{l}^{-1}$), while the anvil particle concentration is only reduced by 32 % (i.e., from $3017\,\mathrm{l}^{-1}$ to $2059\,\mathrm{l}^{-1}$). However, the total number concentration of anvil particles removed by the algorithm ($958\,\mathrm{l}^{-1}$) is an order of magnitude greater than the synoptic cirrus value ($98\,\mathrm{l}^{-1}$). Thus, reporting only the multiplicative factor in the synoptic cirrus case can lead readers to assume that the order of magnitude concentration enhancement due to shattering could also apply to other cases, leading to erroneous conclusions.

The data shown in Fig. 12 also beg a question: why, with roughly the same total mass in each size distribution, does shattering in the anvil regime appear to produce 10 times the concentration of shattered particles? Fig. 13, which shows the anvil and synoptic cirrus size distributions as a function of mass, provides some insight. While the total mass in particles $> \sim 100\,\mu\mathrm{m}$ is roughly the same in both size distributions, there is significantly more mass in sizes $> 1\,\mathrm{mm}$ in the anvil compared to the synoptic cirrus. Also, as shown in several previous studies, and the 2D-S images in Fig. 12, the mass distribution in synoptic cirrus is dominated by bullet rosette shapes, while anvils are typically composed of plates, aggregates of plates and columns (Connolly et al., 2005; Lawson
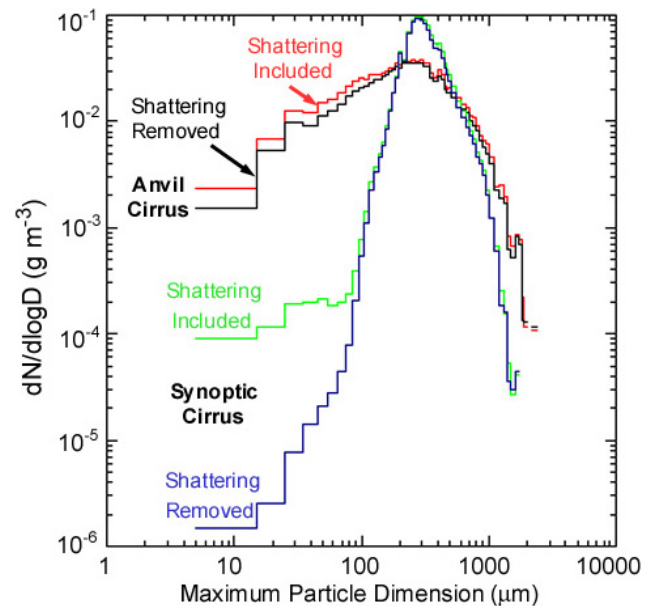
et al., 2006b, 2010; Protat et al., 2011). In addition, Connolly et al. (2005) show that mid-latitude anvils often contain aggregated chains of small plates that could easily break apart when shattered. The observations in Figs. 12 and 13 further emphasize the complexity of the shattering issue and the need for more detailed study, including systematic studies of the shattering characteristics of particles with different sizes and shapes.

4 Summary and discussion

The effects of ice particles shattering on the tips of the 2D-S optical array probe, referred to in this paper as "shattering", are investigated. While shattering has been known for over 35 yr, under certain cloud conditions the magnitude of the contribution of shattered particles can be significant. NASA GRC supplied high-speed video photography in the Cox & Company icing tunnel of ice particles shattering on the tips of cloud particle probes. Korolev et al. (2010a) show that ice particles a few hundreds of microns in size shatter into hundreds of small ice particles with sizes that range from about 10 to 100 μm. As suggested from the comparison of 2D-S particle images in Fig. 5 and size distributions in Figs. 6, 10, 12 and 13, the large majority of these particles are in the size range from 10 to 50 μm (or perhaps even smaller).

Two techniques are currently used to reduce the effects of shattering: (1) probe tips designed to reduce the number of shattered ice particles that enter the sample volume, and (2) algorithms that remove shattered particles in post processing, mainly based on the observation that the shattered

particles are much more closely spaced than natural ice distributions.

Korolev et al. (2010b) report results from analysis of 2D-C and CIP data collected from a field campaign (AIIE) that was designed to evaluate the effects of shattering on cloud particle probes. 2D-C and CIP probes, each with standard tips and tips modified by Korolev[6] were flown side-by-side on the Canadian CV-580. The results show that the modified probe tips were more effective reducing shatterers than post-processing with an arrival time algorithm.

Two 2D-S probes, one with and one without modified probe tips, were flown side-by-side on the SPEC Learjet in the SPARTICUS field project. The modified probe tips were designed with the assistance of Korolev, and are based on theory and knowledge learned from the icing tunnel videography. Analysis of data collected in large aggregates shows that the modified 2D-S probe tips substantially reduce the number of small (shattered) particles; however, post-processing with the arrival time algorithm is more effective, whether applied to the probe with modified or unmodified tips. This is a different result than Korolev et al. (2010b) obtained for the 2D-C and CIP probes.

Korolev et al. (2010a) discuss a possible explanation for the apparent ineffectiveness of the arrival time approach when applied to the 2D-C and CIP probes. Due to the (50 μm to 100 μm) effective size resolution of the CIP and 2D-C, the imagery may miss many of the small shattered particles, producing large gaps that defeat the arrival time algorithm, and/or groups of small particles that are blurred together and appear as one larger particle. The explanation offered by Korolev et al. (2010a) is that it may appear that one (shattered) particle passes through the sample volume and is counted as a real particle. Because depth of field and thus sample volume are inversely proportional to the square of particle size, the one event generates a much higher concentration than does a large particle. The faster time response and greater effective size resolution of the 2D-S probe may enable it to more accurately reproduce particle spacing in a burst of shattered particles, which may make its particle arrival time algorithm more effective.

Results from SPARTICUS, ISDAC, AIIE and MACPEX show that post-processing 2D-S data with the arrival time algorithm (see Appendices A and B) is very effective in minimizing the effects of shattered ice particles. For the first time, measurements from major field programs (e.g., SPARTICUS, TC4, MACPEX) show vertical profiles of ice particle concentration in deep ice clouds (anvils and deep cirrus) that are consistent with physical arguments and numerical models. That is, relatively high concentrations of small ice near cloud top with decreasing concentration of small ice toward cloud base. Data from previous field campaigns (e.g., Lawson et al., 2006b) show increasing concentrations of small ice toward cloud base due to shattering on the older probes. A comparison of 2D-S particle concentrations from MACPEX in synoptically generated cirrus and a convectively generated anvil also more closely represent results from physical arguments and numerical simulations.

The effect of shattering on the second (extinction) and third (ice water content) moments of a cloud particle size distribution can be either minimal, or significant, depending on the instrument, cloud conditions and application of the measurements. The worse situation appears to be when scattering probes, such as the FSSP and the cloud and aerosol spectrometer (CAS), with tubular inlets, are used to measure ice particles in environments with high mass concentrations of large ice. Jensen et al. (2009) suggests that measurements under these conditions significantly skew the second moment of the size distribution, which generates the potential for misleading radiative computations. Ice water content is not as strongly affected as extinction, but significant errors can occur, such as suggested when an FSSP is used to measure small ice particles near the bases of deep cirrus clouds (Lawson et al., 2006b), or when a CAS is used to measure small particle concentration in thunderstorm anvils (Garrett et al., 2005; Fridlind et al., 2004).

All of the shattering results presented here are based on analyses of a few cases, using only three research aircraft, and in a limited number of cloud conditions and flight configurations. Results of the effects of shattering from the SPARTICUS, AIIE, ISDAC and MACPEX projects cannot be considered comprehensive or statistical. A statistical analysis was not possible with the available dataset and was not the focus of this paper. The takeaway message is that the limited dataset indicates that a post-processing algorithm based mainly on particle arrival times is more effective than modified 2D-S probe tips in reducing the effects of shattering. This result differs from analysis of a shattering analysis reported by Korolev et al. (2011b), who found that modified probe tips were more effective than a particle arrival time algorithm in reducing shattering on the CIP and 2D-S probes.

Korolev et al. (2011b) suggest that, based on high-speed video in an icing tunnel, several factors appear to influence the amount of shattering on the inlets and tips of optical cloud particle probes. We suggest that factors that could potentially influence shattering include the probe geometry, time response, size resolution, probe installation on the aircraft, aircraft speed and angle of attack, ice particle size, type, air density and temperature. A comprehensive documentation of the results of shattering will likely require a comprehensive set of flight programs that address these variables. It is likely that estimates of the probability that one shattered ice particle will pass through a probe sample volume, thereby defeating any arrival time algorithm, will require analysis of high-speed, in-flight video.

---

[6] See footnote # 2.

5 Major conclusions

– The effects of ice particles shattering on the tips of 2D-S probes are reduced by modified tips based on the design of Korolev[7], and by post-processing based on an inter-arrival time algorithm (Appendices A and B). However, the inter-arrival time algorithm appears to be more effective than the modified tips with applied to 2D-S data, although use of both techniques is synergistic and recommended. This is a different result than obtained by Korolev et al. (2010b) from the AIEE field campaign, where it is reported that modified tips on CIP and 2D-C probes are more effective than an arrival time algorithm in reducing the effects of shattering.

– When compared to measurements from previous field campaigns that used older cloud particle probes, 2D-S data (with shattering removed) collected in recent (i.e., TC4, SPARTICUS, MACPEX) field campaigns show results that are consistent with physical arguments and numerical simulations. For example, ice particle concentrations in synoptic cirrus are two orders of magnitude less than anvil cirrus, even though total mass concentrations are similar in the regions selected for this analysis. Also, the vertical distribution of small ice particles in deep ice clouds decreases with distance from cloud top while the total mass of ice increases.

– A rigorous quantification of the effects of ice particles shattering on the inlets and tips of optical cloud particle probes is a complicated undertaking, because shattering is contingent on many factors that are a function of the probe, aircraft and environmental properties. However, Figs. 7 and 9, and other scatter plots of this type found in the literature, provide a methodology that forms a crude quantification of the upper bound of the effects of shattering. A comprehensive experiment with perhaps high-speed, in-flight video and extensive measurements in varying cloud regimes and aircraft configurations could shed more light on the physical processes involved in shattering, and also form the basis for statistical analysis.

Appendix A

Software processing of 2D-S Data

Processing of 2D-S image data is a complex process that has evolved based on both theoretical and empirical approaches. Image analysis and derived products include the convolution of multiple algorithmic processes. The convolution of algorithms includes software techniques that make adjustments to particle concentration and size that are used in both the basic processing and removal of shattered particles. Thus, there is crossover of some techniques from one process to another (and consequently from Appendix A to Appendix B, and vice versa). The processing can loosely be divided into three broad steps:

– Various methods to determine "characteristic" lengths, L_i, and areas, A_i, of an image.

– Removal of what are called here "spurious" events (also referred to as artifact rejection), which can include electronic noise, optical contamination, particle shattering and splashing effects.

– Various methods, M_i, of estimating the bulk physical parameters; concentration, extinction, and mass as functions of size. These include correction for diffraction effects based on the Korolev (2007) methodology and adjustments to sample volume as a function of particle size.

These algorithmic processes require the introduction of various parameters that are defined throughout this Appendix and in Appendix B.

There are several different ways that L_i can be measured. Figure A1 is a schematic depicting four measures of image length used in 2D-S analysis. L_1 is the number of slices (pixels in the direction of travel) for which a particle event lasted. L_2 is the number of shaded photodiodes (pixels in the direction along the array) for the slice for which the same quantity is maximized. L_4 is the number of diodes between, and including the shaded end diodes, for the slice that maximizes the same quantity. L_5 is the distance between (and including) the shaded end diodes considering all of the slices together.[8] The appropriate selection of L_i depends on the size and type of particles that are being imaged. For example, if particle sizes exceed the (1.28 mm) viewing area of the 2D-S, use of L_2 would limit the maximum particle size to 1.28 mm, whereas use of L_1 would provide a one-dimensional measurement of particles of any length, providing any part of the particle remained in the viewing area.

Several other size parameters are used in processing an image. L_7 is the diffraction-corrected length for out-of-focus ("donut") images based on Korolev (2007). A_s is the number of occulted pixels for the entire image (summed over all slices). A_t is the total number of pixels (occulted or not) contained within an image, which was developed by Korolev and is used in the Korolev (2007) diffraction-correction method.

The accepted particles are binned according to size. The size bin's edges are: [5, 15, 25, 35, 45, 55, 65, 75, 85, 95, 105, 115, 125, 135, 145, 155, 165, 175, 185, 195, 205, 225, 245,

---

[7] See footnote #2.

[8] Note that the numbering of the "L" lengths is not consecutive because "L" lengths using other techniques were considered and subsequently dismissed. It was not efficient to re-number "L" lengths in the software code and this document is intended to be consistent with the actual code.
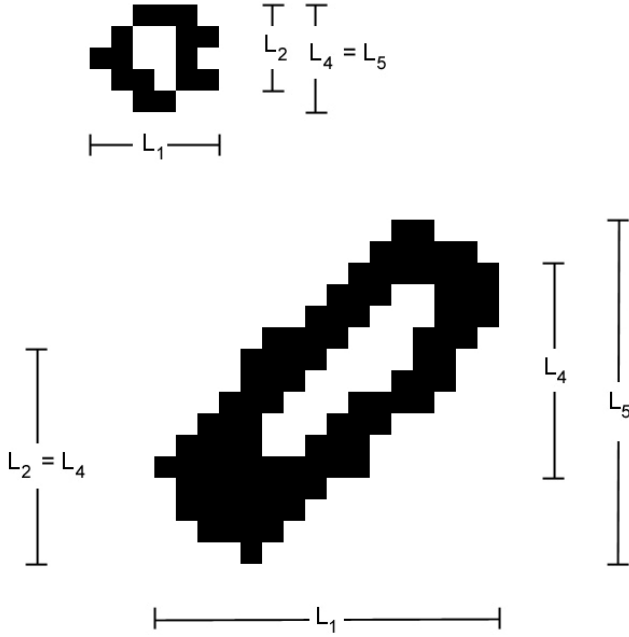
Fig. A1. Two example particle images designed to demonstrate the four measures of image size described in this Appendix.

265, 285, 305, 325, 345, 365, 385, 405, 425, 465, 485, 505, 555, 605, 655, 705, 755, 805, 855, 905, 955, 1005, 1105, 1205, 1305, 1405, 1505, 1605, 1705, 1805, 1905, 2005, 2205, 2405, 2605, 2805, 3005, 3205, 3405, 3605, 3805, 4005, 4205, 4405, 4605, 4805, 5005, 6005, 6505, 7005, 7505, 8005, 8505, 9005, 9505, 10005, 10505, 11005, ∞].

Next we present general equations for calculating bin particle concentration, bin particle area assuming spheres, bin particle area not assuming spheres, bin liquid water content (LWC) and bin ice water content (IWC). The adjustment factor SV_{adj} and sample volume (SV) are defined in specific terms later in Appendix B and below, respectively.

The general equation for a bin's concentration is:

$$\frac{\#_{counts}}{(SV \times BW)} \tag{A1}$$

where $\#_{counts}$ is the number of particles counted in that size bin, BW is the width of the size bin, and SV is the sample volume, defined below according to the method used.

The general equation for a bin's particle projected area assuming spheres is:

$$\frac{\sum \frac{\pi L^2}{4}}{(SV \times BW)}. \tag{A2}$$

where the sum is over the diameters (L) in that size bin which have been appropriately scaled to physical units.

The general equation for a bin's particle projected area not assuming spheres is:

$$\frac{\sum (A_s \times d_{slice} \times d_{diode})}{(SV \times BW)}. \tag{A3}$$

where d_{slice} is the pixel size in the TAS direction and should equal 0.01 mm (10 μm), but could differ if the actual aircraft TAS exceeds the maximum clock speed, or if an incorrect TAS is sent to the probe during data acquisition. d_{diode} is the pixel size along the array, which is 0.01 mm (10 μm) for the 2D-S.

The general equation for a bin's LWC is:

$$\frac{\sum \rho_{liq} \frac{\pi L^3}{8}}{(SV \times BW)}. \tag{A4}$$

where the sum is over the diameters (L) in that size bin which have been appropriately scaled to physical units, ρ_{liq} is the density of liquid water.

The general equation for a bin's IWC is:

$$\frac{\sum (M_{ice})}{(SV \times BW)}. \tag{A5}$$

where the sum is over all the particles with L in that size bin and M_{ice} is found as the smaller of the two estimates; $\frac{1}{6} \times \pi \times L^3 \times \rho_{ice}$ (where L has been scaled to physical units of mm and ρ_{ice} is the bulk density of ice) and $0.115 \times A_s^{1.218}$ (where A_s has been scaled to physical units of mm^2 and M_{ice} is in mg).

Sample volumes are calculated according to the method (M_i) used as:

M_1, which uses the length parameter along the direction of travel (L_1) to determine size and includes images that touch an edge:

$$SV_1 = \left[TAS \times \Delta t \times \left(N_{diodes} - 1 + L_1 \times \frac{d_{slice}}{d_{diode}} \right) \right. \\ \left. \times d_{diode} \times DOF \right] \times SV_{adj} \tag{A6}$$

where DOF is the smaller of d_{ww} and d_{DOF}, $d_{ww} = 63$ mm (6.3 cm) is the window to window distance between the probe arms, $d_{DOF} = F_{DOF} \times L_1^2 \times d_{slice}^2$ where $F_{DOF} = 5.13 \times 10^{-3}$ (mm μm^{-2}), N_{diodes} is the number diodes in the array, which is 128 for the 2D-S. SV_{adj} is an adjustment to the sample volume used to account for valid particle events that are rejected by the artifact rejection algorithm(s), see Appendix B. Sample volume (SV) will be in liters if the DOF and d_{diode} are in mm and the speed of air through the probe sample area (TAS) is in m s^{-1}, and the "live time" (Δt) is in seconds. Note that for a given processed period, Δt will be less than that period due to probe "dead time". "dead time" is essentially time when the probe is not able to detect new events, such as when a particle is already being detected or when the data transfer rate has been exceeded and the probe goes into "overload".

M_2, which uses the length parameter L_4 to determine size and excludes images that touch an edge:

$$SV_1 = [TAS \times \Delta t \times (N_{diodes} - 1 - L_4) \times d_{diode} \times DOF] \\ \times SV_{adj} \tag{A7}$$

where

$$d_{\mathrm{DOF}} = F_{\mathrm{DOF}} \times L_4^2 \times d_{\mathrm{diode}}^2 \qquad (A8)$$

M_4 attempts to address the issue of mis-sizing out of focus images by using the length parameter L_7 to determine size. It also excludes images that touch an edge. The sample volume uses the same equations as for M_2 except that L_4 is replaced with L_7.

M_6 also addresses the issue of out of focus images by using a combination of M_1 and M_2 but for in focus particles only. In focus particles are defined as the ration of A_s to $A_t > 0.9$. It uses M_2 up to 265 μm in size and M_1 for greater than 325 μm. The bins between 265 to 325 use weighted means of M_1 and M_2. For M_6, $F_{\mathrm{DOF}} = 2.07 \times 10^{-3}$ (mm μm^{-2}).

The 2D-S data presented and discussed in this paper were processed using M_4 (that includes the Korolev (2007) diffraction correction) for image sizes out to 365 μm, and M_1 for images larger than 445 μm. The bins between 365 to 445 use weighted means of M_1 and M_4. The rationale for this is that particles <400 μm can move far enough from the object plane to produce "donuts" that require diffraction correction, while particles >400 μm do not produce donuts because the probe arms limit the distance from the object plane to less than that required to produce donuts. Also, smaller particles tend to be more spherical in shape and the Korolev (2007) corrections are designed for spherical particles. Lastly, M_1 does not restrict particle size in the direction of particle travel and M_4, which uses L_2 as its initial measurement, is size limited to 1.28 mm.

To implement the Korolev (2007) diffraction correction the Poisson spot area is estimated from $A_{\mathrm{spt}} = A_t - A_s$. The square root of the ratio of A_{spt} to A_t is used as an estimate of the ratio of the diameter of the spot size to the outer diameter of the image. These values are then used together with a table produced by Korolev, following Korolev (2007), to determine an estimated actual diameter of a (spherical) particle. After testing the algorithm on various glass beads of known size in the laboratory the following adjustments were made:

1. Instead of the theoretically appropriate 50 % shadow depth table, we use the 40 % shadow depth table. This is a compromise. For each bead size a different table worked best.

2. We do not allow the algorithm to increase the particle size.

3. If the image is sufficiently in focus (ratio of A_s to $A_t > 0.9$) we do not make any correction.

Fig. B1. Examples of line plus dot patterns caused by noisy photodiodes.

Appendix B

Removing spurious 2D-S Events

2D-S raw data include spurious events, also called artifacts. These are primarily from noisy photodiodes and from splashing or shattering of precipitation. Algorithms used to remove the majority of these spurious events, while retaining the majority of the valid images, are described in this Appendix. There are five quasi-independent steps to the "cleaning" algorithm implemented via two loops through the data:

B1   First Loop

1. Test for noise via line and dot patterns.

2. Test for noise via statistics of particle center locations.

3. Test for roundness. Applied in liquid water clouds only.

4. Test for splashing and shattering events based on black and white area considerations.

B2   Second Loop

5. Test for (ice) shattering and (raindrop) splashing events based on inter-event-distances if the probe is in precipitation.

Note that the algorithms used to remove artifacts from both shattering and splashing are the same, with the exception that a roundness criteria is used in the splashing algorithm. Later in this Appendix we show examples of artifacts from splashing and shattering.

Line plus dot patterns can occur when one or more of the 128 photodiodes (called bits) intermittently exceeds the shadow threshold depth in particle-free air. This "noise" is recognizable if the frequency of the event is sufficient to be captured by the algorithm. Figure B1 shows some examples of noise-generated images appearing in line plus dot patterns.

The noisy bits are eliminated using the following criteria:

1. $(L_1 = A_s)$ and $(L_2 = 1)$ and $(L_1 > 4)$

2. $(A_s \leq 1.35 \text{ X } L_1)$ and $(L_4 = L_5)$ and $(L_1 > 4)$ and $(L_2 = 2)$

3. $(L_1 > 10)$ and $(L_1 > 0.75 \text{ X } A_s)$ and $(L_1 \leq 1.5 \text{ X } A_s)$

4. $(L_4 = L_5)$ and $(A_t > 0.9 \text{ X } L_1 \text{ X } L_5)$ and $(L_2 = 2)$ and $(L_2 \neq L_4)$
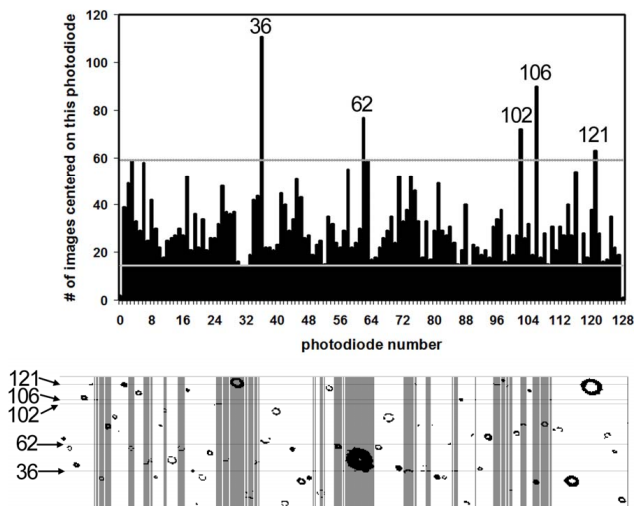
Fig. B2. Example of noisy photodiode data intermixed with good particle data. The images highlighted in grey are rejected. Horizontal lines indicate the location of photodiodes determined to be noisy by the criteria described in the text and exemplified in the particle-center-location distribution shown above.

5. $(L_4 = L_5)$ and $(A_t > 3.0 \, \text{X} \, A_s)$ and $(L_2 = 2)$

6. $(L_4 = L_5)$ and $(A_t > 4.0 \, \text{X} \, A_s)$

L_i ($n = 1, 2, 4, 5,$), A_s and A_t are defined in Appendix A. If any of the six criteria are met, the image is rejected.

The second step of this first cleaning loop is another noisy-diode removal method, based on the statistics of image center locations calculated over 4000 images[9] approximately centered on the image being evaluated. Figure B2 shows an example of data with noisy photodiodes and the distribution of image centers across the array. When a photodiode is noisy, there are more image centers located on that diode than are located on quiet diodes. A photodiode is labeled noisy when it has more particle center locations than the threshold value (TH $= \max(M + 5 \times \sqrt{M}, 1.5)$). Where M is the mean number of image centers per diode across the array, for diodes having more than a minimum number of image center counts. This minimum number is $Mt - 3 \times \sqrt{Mt}$, where Mt is the mean number of image centers per diode across the array, for all diodes. If less than 33 photodiodes satisfy the requirement of having more than Mt counts then M is calculated from all diodes (i.e. $M = \text{Mt}$). Mt and M are recalculated after noisy diodes are identified, ignoring those diodes, and the process

---

[9] The 4000 images include all images, whether rejected by previous steps or not, and is updated every 100 images so that the 4000 images are approximately centered on the current image. If the file contains less than 4000 images then all images are used. 4000 was chosen because of the approximate match between the mean (4000/128 = 31) and the additional amount to reach the threshold ($5 \times \sqrt{31} = 28$)

repeated until no remaining photodiodes exceed the threshold. An image whose center falls on a noisy diode is rejected unless it meets the following criteria:

$(L_1 \geq 4)$ and $(L_5 \geq 4)$ and $(L_2 \geq 3)$ and $(A_s \geq 0.5 \times A_t)$ and $(L_1 < 10 \times L_2)$.

A test for roundness is performed and used in water clouds. An image is determined to be round if $L_1 \geq \text{TH}_{\text{rnd}} \times L_5$ and $L_5 \geq \text{TH}_{\text{rnd}} \times L_1$. An exception is made for the very large images that do not fit within the array. If $L_5 > 50$ (500 μm) then an image is determined to be round if $L_1 \geq \text{TH}_{\text{rnd}} \times L_5$. i.e., an image is determined to be round if $L_1 \geq \text{TH}_{\text{rnd}} \times L_5$ and $(L_5 \geq \text{TH}_{\text{rnd}} \times L_1$ or $L_5 > 50)$. For water clouds $\text{TH}_{\text{rnd}} = 0.5$.

The larger a valid image is the greater the percentage of shaded pixels. Shattering and splashing effects often create large images that have lower percentages of shaded pixels than valid images (see example in Fig. B3). The follow criteria are used to eliminate such spurious images:

1. $(L_5 > 10$ or $L_1 > 10)$ and $(A_t > 3.0 \, \text{X} \, A_s)$

2. $(L_5 > 15$ or $L_1 > 15)$ and $(A_t > 2.5 \, \text{X} \, A_s)$

3. $(L_5 > 20$ or $L_1 > 20)$ and $(A_t > 2.0 \, \text{X} \, A_s)$

If any of these four criteria is met, the image is rejected.

The final step is another loop through the data to calculate the inter-particle spacings and reject particles that are close together. This algorithm is only performed if the current precipitation status is "yes". The current precipitation status is "yes" if there is one or more particle(s) with L_7 > 100 μm in 10 000 particles accepted by the first two cleaning steps, centered approximately on the current particle. It is approximately centered because the precipitation status is updated only every N particles, to improve speed. The value of 100 μm was chosen because particles smaller than this are less likely to be a major contributor to shattering and splashing.

The current mean inter-particle time (aveW8), is also updated every N particles and calculated as the average inter-particle time between 10 000 images, accepted by the previous four cleaning steps, centered approximately on the current particle. All the accepted particles in the previous second are used instead of 5000 particles if there are less than 5000 particles in the previous second, similarly for the following 5000 particles or second. If aveW8 > 40 000 then $C_1 = 2000$ and $C_2 = 8000$. If aveW8 < 40 000 then $C_1 = 0.05$ X aveW8 and $C_2 = 0.2$ X aveW8. A particle is rejected if the precipitation status[10] is "yes" and either: (a) the particle's inter-particle time or the following particle's inter-particle time is less than C_1 or (b) both the particle's inter-particle

---

[10] The precipitation status and current mean waiting time are updated every N particles, where N is the smaller of N_1 and N_2, where N_1 is the number of so far accepted particles in the previous 0.1 s and N_2 is the number of so far accepted particles in the following 0.1 s.
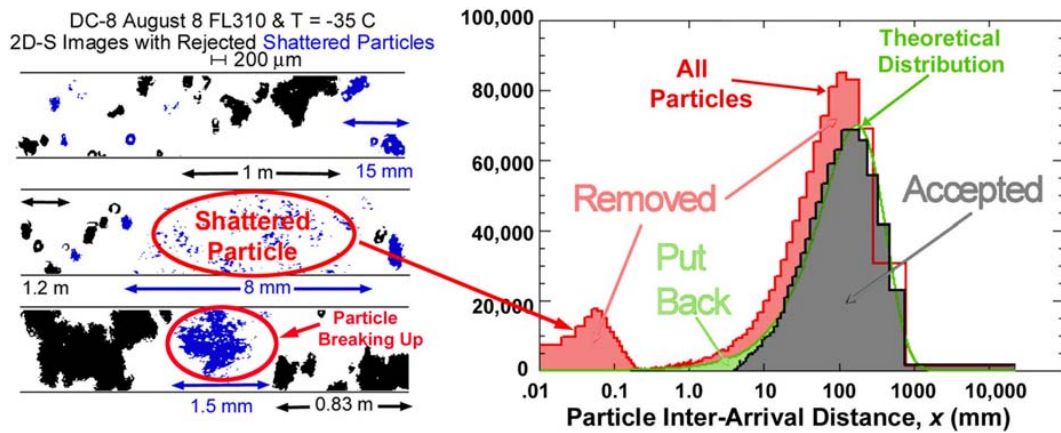
Fig. B3. Example of (left) 2D-S images in ice with particles in blue identified as artifacts using the algorithms described in this Appendix, and (right) plot of particle events versus inter-arrival distance showing (in red) the inter-particle distances before removing shatterers, (in black-grey) the remaining ("Accepted") particles' inter-particle distances after "Removing" shatterers, and (in green) an exponential distribution with the same mean as the after-shattering removal distribution, for comparison (labeled "Theoretical Distribution"). For the sake of simplicity in nomenclature, the difference between the black and green distributions is what is labeled "Put Back", but in reality the results are adjusted by the factor SV_{adj}, as described in the text.

time and the following[10] particle's inter-particle time are less than C_2[11].

An exception occurs when a particle has $L_1 > 10$ and the inter-particle time for that particle (or the next particle) is less than 10, and the previous particle (next particle) has area <10. In these cases, the previous particle (next particle) is considered a diffraction satellite and is ignored. i.e. the previous (next), non-satellite, particle's inter-particle time is used.

A variable, SV_{adj}, is calculated for each image in the following manner. SV_{adj} is 1 if precipitation status is "no". When precipitation status is "yes" a new true average inter-particle time is calculated. TaW = the average inter-particle time of particles accepted by all the steps minus C_1. Assuming a true waiting time distribution with a mean of TaW, then $1 - e^{-C_1/TaW}$ is the probability of, or fraction of events with, inter-arrival times less than C_1. $1 - e^{-2C_1/TaW}$ is the fraction of events eliminated due to the first criterion, leaving $e^{-2C_1/TaW}$ not eliminated by the first criterion. Of those, a fraction $\left(1 - e^{-C_2/TaW}\right)^2$ are eliminated by the second criterion. Thus, the fraction of events eliminated by the criteria given a true waiting time distribution with mean of TaW is

$$k = 1 - e^{-2C_1/TaW} + e^{-2C_1/TaW}\left(1 - e^{-C_2/TaW}\right)^2, \quad \text{(B1)}$$

---

[11] Events eliminated by steps 1 and 2 are not considered as following events. If the next event has been eliminated by either step 1 or step 2 then the next event, not eliminated by step 1 or step 2 is used and its inter-particle time is the time from the last event not eliminated by step 1 or step 2. Similarly, the current particles wait time must be from the previous event not rejected by step 1 or step 2. i.e., the wait times for particles not rejected by step 1 or step 2 are recalculated at this point.
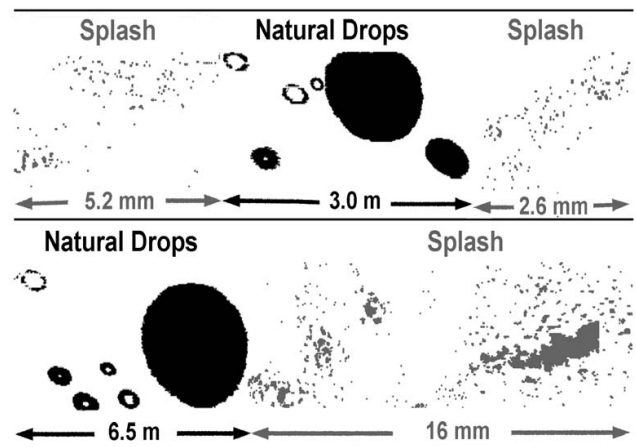

Fig. B4. Example of 2D-S images in raindrops with particles in grey identified as artifacts using the algorithms described in this Appendix (from Baker et al. 2009).

$SV_{adj} = \frac{1}{1-k}$ (but capped at 1.11) is used elsewhere in the algorithms for calculating concentrations, area, etc., to increase the weight of each accepted particle to account for those good particles rejected by the inter-particle time criteria. See Appendix A for details.

Figure B3 shows an example of 2D-S images in ice, identifying those images that have been removed via the algorithms described in Appendix B. The panel on the right in Fig. B3 shows (in red) the inter-particle distances before removing shatterers, (in black-grey) the remaining particles' inter-particle distances after removing shatterers, and (in green) an exponential distribution with the same mean as the after-shattering removal distribution, for comparison (labeled

Theoretical Distribution in the figure). Note, these exponential and near exponential curves have apparent maxima only because they are plotted dN/dlog(N). For the sake of simplicity in nomenclature, the difference between the black and green distributions is what is labeled "Put Back" in the figure, but in reality the results are adjusted by the factor SV_{adj}, as described above.

For comparison purposes, Fig. B4 shows an example of small drops generated from raindrops splashing on the tips of the 2D-S. The "splashers" are shown to highlight the similarity between ice particle "shatterers" (see Fig. B3) and raindrop "splashers" seen in 2D-S images. This does not imply that the physics of ice particles shattering on probe tips are identical to raindrops splashing on probe tips, but instead to show that the resulting 2D-S images are very similar, suggesting that the particle inter-arrival time algorithm can be effectively applied in both cases.

Appendix C

Description of 2D-S Probe Tips

As described in the Introduction to this paper, the probe tips on the 2D-S were modified based on information communicated from Alexei Korolev to SPEC engineers. The 2D-S probe that is termed the "standard" or "unmodified" probe in this paper had tips that were designed by SPEC to minimize shattering, but without benefit of information later provide by Korolev. The 2D-S with "modified" probe tips was designed and fabricated based on information that Korolev delivered in person to SPEC engineers. Further, the modified probe tips were first applied as a retrofit to the standard probe by fastening adapter tips onto the existing probe arms. Figure C1. shows photographs of the standard probe tips and the standard probe tips with the adapters. 2D-S data from the ISDAC field campaign and from the "standard" probe during the SPARTICUS field campaign were collected with standard probe tips. Data collected using a 2D-S probe with tips retrofitted with adapters were collected in the AIIE field campaign and by the modified probe during SPARTICUS. Lastly, new probe arms and tips based on the design used in fabricating the adapter tips were fabricated and installed on a new 2D-S probe for the MACPEX field campaign. A photograph of the 2D-S probe tips used in the MACPEX project and an engineering drawing showing plan and profile views of the modified probe tips are also shown in Fig. C1.
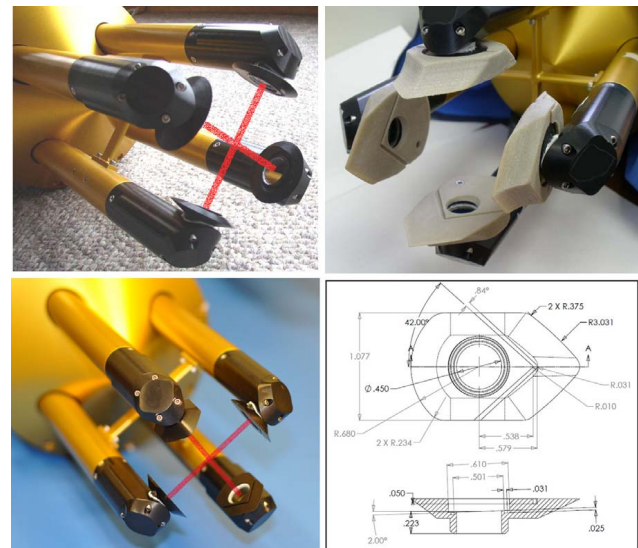
Fig. C1. (top left) Photograph of "standard" (unmodified) 2D-S probe tips used in ISDAC and by the standard probe in SPARTICUS. (upper right) Photograph of 2D-S probe with adapter tips fitted onto the standard probe arms, which was used in the AIIE field campaign and by the modified probe during SPARTICUS (note that the outer surfaces of the adapter tips have rime ice on them). (lower left) Photograph of the 2D-S probe tips that are designed based on the adapter tips shown at the upper right, but are integrated with the 2D-S probe arms; these tips were used in the MACPEX project. (lower right) Engineering drawing showing shape and dimensions of the modified probe tips.

References

Baker, B. A., Korolev, A., Lawson, R. P., O'Connor, D., and Mo, Q.: Drop Size Distributions and the Lack of Small Drops in RICO Rain Shafts, J. Appl. Meteorol., 48, 616–623, 2009.

Baumgardner, D., Jonsson, H., Dawson, W., O'Connor, D., and Newton, R.: The cloud, aerosol and precipitation spectrometer: a new instrument for cloud investigations, Atmos. Res., 59–60, 251–264, 2001.

Comstock, J. M., Lin, R. F., Starr, D. O., and Yang, P.: Understanding ice supersaturation, particle growth, and number concentration in Cirrus clouds, J. Geophys. Res, 113, D23211, doi:10.1029/2008JD010332, 2008.

Connolly, P. J., Saunders, C. P. R., Gallagher, M. W., Bower, K. N., Flynn, M. J., Choularton, T. W., Whiteway, J., and Lawson, R. P.: Aircraft observations of the influence of electric fields on the aggregation of ice crystals, Q. J. Roy. Meteorol. Soc., 18, 1695–1712. 2005.

Cooper, W. A.: Cloud physics investigation by the University of Wyoming in HIPLEX 1977, Bureau of Reclamation Rep., AS, 119, 321 pp., 1978.

Field, P. R., Wood, R., Brown, P. R. A., Kaye, P. H., Hirst, E., Greenaway, R., Smith, J. A.: Ice particle interarrival times measured with a Fast FSSP, J. Atmos. Oceanic Technol., 20, 249–261, 2003.

Field, P. R., Heymsfield, A. J., and Bansemer, A.: Shattering and Particle Interarrival Times Measured by Optical Array Probes in Ice Clouds, J. Atmos. Oceanic Technol., 23, 1357–1370, 2006.

Fridlind, A. M., Ackerman, A. S., Jensen, E. J., Heymsfield, A. J., Poellot, M. R., Stevens, D. E., Wang, D., Miloshevich, L. M., Baumgardner, D., Lawson, R. P., Wilson, J. C., Flagan, R. C., Seinfeld, J. H., Jonsson, H. H., VanReken, T. M., Varutbangkul, V., and Rissman, T. A.: Evidence for the predominance of midtropospheric aerosols as subtropical anvil nuclei, Science, 303, 718–722, 2004.

Gardiner, B. A. and Hallett, J.: Degradation of in-cloud forward scattering spectrometer probe measurements in the presence of ice particles, J. Atmos. Oceanic Technol., 2, 171–180, 1985.

Garrett, T. J., Navarro, B. C., Twohy, C. H., Jensen, E. J., Baumgardner, D. G., Bui, P. T., Erber, H., Herman, R. L., Heymsfield, A. J., Lawson, P., Minnis, P., Nguyen, L., Poellot, M., Pope, S. K., Valero, F. P. J., and Weinstock, E. M.: Evolution of a Florida Cirrus Anvil, J. Atmos. Sci., 62, 2352–2372, 2005.

Gayet, J.-F., Brown, P. R., and Albers, F.: A comparison on in-cloud measurements obtained with six PMS 2D-C probes, J. Atmos. Ocean. Tech., 10, 180–194, 1993.

Gayet J.-F., Auriol, F., Minikin, A., Ström, J., Seifert, M., Krejci, R., Petzold, A., Febvre, G., and Schumann, U.: Quantitative measurement of the microphysical and optical properties of cirrus clouds with four different in situ probes: Evidence of small ice crystals, Geophys. Res. Lett., 29, 2230–2233, 2002.

Jensen, E. J., Lawson, P., Baker, B., Pilson, B., Mo, Q., Heymsfield, A. J., Bansemer, A., Bui, T. P., McGill, M., Hlavka, D., Heymsfield, G., Platnick, S., Arnold, G. T., and Tanelli, S.: On the importance of small ice crystals in tropical anvil cirrus, Atmos. Chem. Phys., 9, 5519–5537, doi:10.5194/acp-9-5519-2009, 2009.

Kärcher, B. and Ström, J.: The roles of dynamical variability and aerosols in cirrus cloud formation, Atmos. Chem. Phys., 3, 823–838, doi:10.5194/acp-3-823-2003, 2003.

Knollenberg, R. G.: The optical array: An alternative to scattering or extinction for airborne particle size determination, J. Appl. Meteor., 9, 86–103, 1970.

Korolev, A. V.: Reconstruction of the sizes of spherical particles from their shadow images. Part I: Theoretical considerations, J. Atmos. Oceanic Technol, 24, 376–389, doi:10.1175/JTECH1980.1, 2007.

Korolev, A. V. and Isaac, G. A.: Shattering during sampling by OAPs and HVPS. Part 1: Snow particles, J. Atmos. Oceanic Technol., 22, 528–542, 2005.

Korolev, A., Emery, E., Strapp, W., Cober, S., Isaac, G., and Wasey, M.: Small ice particle observations in tropospheric clouds: fact or artifact?, Recorded presentation; AMS 13th Cloud Physics Conference; Portland OR, 28 June–2 July 2010 (https://confex.webex.com/cmp0306lc/webcomponents/widget/playback.do?siteurl=confex&playback=playback&fileName=http://ams.confex.com/recording/ams/13CldPhy13AtRad/wrf/free/4db77adf5df9fff0d3caf5cafe28f496/paper171437_3.wrf), 2010a.

Korolev, A. V., Emery, E. F., Strapp, J. W., Cober, S. G., Isaac, G. A., Wasey, M., and Marcotte, D.: Small ice particles in tropospheric clouds: fact or artifact? Airborne Icing Instrumentation Evaluation Experiment, doi:10.1175/2010BAMS3141.1, early release available at: http://journals.ametsoc.org/doi/pdf/10.1175/2010BAMS3141.1, 2010b.

Lawson, R. P., O'Connor, D., Zmarzly, P., Weaver, K., Baker, B. A., Mo, Q., and Jonsson, H.: The 2D-S (Stereo) Probe: Design and preliminary tests of a new airborne, high speed, high-resolution particle imaging probe, J. Atmos. Oceanic Technol., 23, 1462–1477, 2006a.

Lawson, R. P., Baker, B. A., Pilson, B., and Mo, Q.: In Situ observations of the microphysical properties of wave, cirrus and anvil clouds. Part II: Cirrus Clouds, J. Atmos. Sci., 63, 3186–3203, 2006b.

Lawson, R. P., Jensen, E., Mitchell, D. L., Baker, B., Mo, Q., and Pilson, B.: Microphysical and radiative properties of tropical clouds investigated in TC4 and NAMMA, J. Geophys. Res., 115, D00J08, doi:10.1029/2009JD013017, 2010.

McFarquhar, G. M., Um, J., Freer, M., Baumgardner, D., Kok, G. L., and Mace, G.: The importance of small ice crystals to cirrus properties: Observations from the Tropical Warm Pool International cloud Experiment (TWP-ICE), Geophys. Res. Lett., 57, L13803, doi:10.1029/2007GL029865, 2007.

Protat, A., McFarquhar, G. M., Um, J., and Delanoë, J.: Obtaining Best Estimates for the Microphysical and Radiative Properties of Tropical Ice Clouds from TWP-ICE In Situ Microphysical Observations, J. Appl. Meteor. Climatol., 50, 895–915, doi:10.1175/2010JAMC2401.1, 2011.

Strapp, J. W., Albers, F., Reuter, A., Korolev, A. V., Maixner, U., Rashke, E., and Vukovic, Z.: Laboratory Measurements of the Response of a PMS OAP-2DC, J. Atmos. Oceanic Technol., 18, 7, 1150–1170, 2001.